AN INTRINSIC SENSING RAM EXTRUDER WITH PRESSURE AND VOLUMETRIC FLOW CONTROL FOR LIQUID DEPOSITION MODELING

Mr. Kantawatchr Chaiprabha

จุฬาลงกรณ์มหาวิทยาลัย
CHULALONGKORN UNIVERSITY

A Thesis Submitted in Partial Fulfillment of the Requirements
for the Degree of Master of Engineering in Cyber-Physical System
Department of Mechanical Engineering
FACULTY OF ENGINEERING
Chulalongkorn University
Academic Year 2023

เครื่องฉีดแบบแรมสำหรับการขึ้นรูปจากของเหลวที่มีระบบการควบคุมความดันและปริมาตรการไหลและมีระบบตรวจจัดโดยวิสัย

นายกันตวัชร์ ชัยประภา

จุฬาลงกรณ์มหาวิทยาลัย
CHULALONGKORN UNIVERSITY

วิทยานิพนธ์นี้เป็นส่วนหนึ่งของการศึกษาตามหลักสูตรปริญญาวิศวกรรมศาสตรมหาบัณฑิต
สาขาวิชาระบบกายภาพที่เชื่อมประสานด้วยเครือข่ายไซเบอร์ ภาควิชาวิศวกรรมเครื่องกล
คณะวิศวกรรมศาสตร์ จุฬาลงกรณ์มหาวิทยาลัย
ปีการศึกษา 2566

Thesis Title	AN INTRINSIC SENSING RAM EXTRUDER WITH PRESSURE AND VOLUMETRIC FLOW CONTROL FOR LIQUID DEPOSITION MODELING
By	Mr. Kantawatchr Chaiprabha
Field of Study	Cyber-Physical System
Thesis Advisor	RATCHATIN CHANCHAROEN

Accepted by the FACULTY OF ENGINEERING, Chulalongkorn University in Partial Fulfillment of the Requirement for the Master of Engineering

..... Dean of the FACULTY OF ENGINEERING

()

THESIS COMMITTEE

..... Chairman
(GRIDSADA PHANOMCHOENG)

..... Thesis Advisor
(RATCHATIN CHANCHAROEN)

..... Examiner
(NATTAPOL DAMRONGPLASIT)

..... External Examiner
(Pollawat Charoeythornkhajhornchai)

จุฬาลงกรณ์มหาวิทยาลัย
CHULALONGKORN UNIVERSITY

กันตวัชร์ ชัยประภา : เครื่องฉีดแบบแรมสำหรับการขึ้นรูปจากของเหลวที่มีระบบการควบคุมความดันและปริมาตรการไหลและมีระบบตรวจวัดโดยวิสัย. (AN INTRINSIC SENSING RAM EXTRUDER WITH PRESSURE AND VOLUMETRIC FLOW CONTROL FOR LIQUID DEPOSITION MODELING) อ.ที่ปรึกษาหลัก : รัชทิน จันทร์เจริญ

วิทยานิพนธ์นี้นำเสนอการขับเคลื่อนแบบยืดหยุ่นที่สามารถทำการตรวจวัดได้โดยวิสัยในระบบหัวฉีดการขึ้นรูปโมเดลจากของเหลว ระบบขับเคลื่อนสามารถควบคุมการฉีดได้ทั้งการฉีดแบบอัดด้วยความดันและการฉีดแบบอัดด้วยปริมาตร แบบจำลองทางคณิตศาสตร์ถูกสร้างขึ้นเพื่อออกแบบและจำลองการทำงานของหัวพิมพ์ หัวพิมพ์นี้ยังสามารถทำการวัดความดันและอัตราการไหล ซึ่งช่วยเพิ่มความแม่นยำในระหว่างการพิมพ์ นอกจากนั้นแล้วเครื่องพิมพ์ยังสามารถตรวจวัดสมบัติของวัสดุที่นำมาพิมพ์ได้ ซึ่งช่วยให้ได้ข้อมูลเชิงลึกในระหว่างการพิมพ์ ระบบดังกล่าวช่วยพัฒนาการควบคุมความดันและการไหลของวัสดุนอกจากนั้นยังสามารถตรวจวัดและตอบสนองกับสมบัติของวัสดุที่พิมพ์ได้ โดยสรุปแล้วงานวิจัยนี้สามารถช่วยผลักดันประสิทธิภาพในการพิมพ์สามมิติด้วยการฉีดแบบแรม

จุฬาลงกรณ์มหาวิทยาลัย
CHULALONGKORN UNIVERSITY

สาขาวิชา	ระบบกายภาพที่เชื่อมประสานด้วยเครือข่ายไซเบอร์	ลายมือชื่อนิสิต .....
ปีการศึกษา	2566	ลายมือชื่อ อ.ที่ปรึกษาหลัก .....

6570016221 : MAJOR CYBER-PHYSICAL SYSTEM
KEYWORD: Liquid Deposition Modeling, Ram Extrusion, Actuation and Sensing, Viscoelastic Material, Control

Kantawatchr Chaiprabha : AN INTRINSIC SENSING RAM EXTRUDER WITH PRESSURE AND VOLUMETRIC FLOW CONTROL FOR LIQUID DEPOSITION MODELING. Advisor: RATCHATIN CHANCHAROEN

In this dissertation, a ram extruder for liquid deposition modeling (LDM) with a flexible actuation system is proposed. The system allows the command of flow through either pressure or volumetric modes. A mathematical model of the extruder is implemented. The actuation system enables real-time monitoring of pressure and material flow rate, providing benefits for precise control and adjustment during the printing process. Additionally, the system allows for the classification of material viscosity characteristics, offering in-depth information on the material for further analysis of the printing process. The prototype provides the advantage of both pressure and volumetric flow, as well as the ability to assess the material's response. In conclusion, this dissertation enhances the performance of ram extrusion in 3D printing.

จุฬาลงกรณ์มหาวิทยาลัย
CHULALONGKORN UNIVERSITY

Field of Study:	Cyber-Physical System	Student's Signature .....
Academic Year:	2023	Advisor's Signature .....

ACKNOWLEDGEMENTS

Kantawatchr Chaiprabha

จุฬาลงกรณ์มหาวิทยาลัย
CHULALONGKORN UNIVERSITY

TABLE OF CONTENTS

Page

..... iii

ABSTRACT (THAI) iii

.....iv

ABSTRACT (ENGLISH).....iv

ACKNOWLEDGEMENTS.....v

TABLE OF CONTENTS.....vi

Introduction.....1

1.1 Background and Motivation 1

1.2 Objectives of the thesis.....2

1.3 Contributions to the field.....2

1.4 Scope of the thesis 3

1.4 Detailed Research Procedures 4

Research methodology.....5

2.1 The conceptual design 5

2.2 Mathematics.....6

Stability analysis: Lyapunov's second method of stability 8

The measurement and regulation of pressure.....10

The measurement and regulation of volumetric flow rate 11

The assessment of the rheological properties.....11

2.3 Simulation.....12

Controlled voltage source.....12

Rotational Electromechanical converter 13

Resistor.....13

Inductor 13

Electrical reference.....14

Mechanical rotational reference 14
Lead screw 14
Translational friction 14
Translational spring 15
Mass 15
Nonlinear translational damper 15
Mechanical translational reference 16
Current sensor 16
Ideal rotational motion sensor 16
2.4 Hardware Implementation 21
Pressure extrusion 22
3.1 Pressure measurement 22
Pressure observer 22
Pressure sensor 22
Parameter acquisition 23
Effectiveness of pressure measurement 24
3.2 Pressure control 25
Current control 25
Pressure control 27
Effectiveness of pressure control 28
Volumetric flow extrusion 30
4.1 Volumetric measurement 30
Final value theorem 31
Analysis of steady state response from the model 31
Position controller 33
Extrusion experiments 34
5.1 Flushing experiments 34
5.2 Line extrusion experiments 36
Experimental setup 37

จุฬาลงกรณ์มหาวิทยาลัย
Chulalongkorn University

Experimental results 41
5.1 Clog detection experiment 49
Time synchronization 50
Clog enhancement via image processing 53
Experimental result 55
Conclusion 57
REFERENCES 58
VITA 62

จุฬาลงกรณ์มหาวิทยาลัย
CHULALONGKORN UNIVERSITY

Introduction

1.1 Background and Motivation

Additive manufacturing, also known as three-dimensional (3D) printing, is a technology that builds 3D objects by layering materials on top of each other [1, 2]. This enables the creation of complex geometries and customization without expensive tooling, and reduces material waste [3]. Recent advances in materials science, software, and hardware have made it more accessible and cost-effective, leading to a proliferation of applications across industries [4, 5]. This technology enables lightweight, strong, and complex parts, rapid prototyping, and faster time-to-market for new products. Its growing adoption has spurred innovation and new business models, creating opportunities for entrepreneurs and manufacturers [6-8].

Liquid Deposition Modeling (LDM) is a 3D printing technology that deposits paste-like material on build platform to create objects layer-by-layer [9, 10]. For each layer, printing material in the form of paste is extruded onto a build platform through a nozzle, and then cured using certain mechanisms, mostly chemical reaction. This process can be used to produce objects with a wide range of materials, such as polymers, ceramics, and biomatters [11-13]. This technology has great potential for various applications, such as construction, food, and medical [14, 15]. There are three main branches of research in LDM, including rheology, material, and application.

Rheology is the study of the deformation and flow of materials, ranging from elastic solids to viscous liquids [16, 17]. Rheological analysis aims to understand how materials behave under different conditions. This field plays an important role in determining the deformation and flow of printing materials in LDM process [18, 19]. In particular, the majority of the printing materials is viscoelastic material [20, 21]. Rheological models are mathematical equations applicable for describing the rheological behavior of the printing materials [22]. In each rheological model, there are rheological parameters. By determining rheological parameters, the optimization of printing parameters for specific printing conditions and materials can be systematically proceeded, instead of optimizing by trial-and-error tuning [23, 24]. Mechanical analogies are widely used to represent rheological viscous and elastic behavior [25, 26]. A damper depicts viscous behavior, while a spring portrays elastic behavior. Several rheological models were elaborated following this concept. Maxwell model [27] is a widespread model that was developed based on these analogies, to handle viscoelastic fluid behavior. Another extensive model that follows the mentioned analogies is Voigt model [27], which describes only viscoelastic solid behavior. Based on such rheological models, Burgers model [28] was elaborated to describe viscoelastic complex behavior.

Despite the existence of various rheological models, determining rheological parameters remains a significant practical challenge. This issue is compounded by the fact that these parameters are inherently time-dependent and exceptionally sensitive to disturbances, particularly variations in material temperature [29-31]. Furthermore, the viscoelastic properties of materials vary from one location to another, making it impractical to possess a complete understanding of their behavior across all points within the material.

The most viable approach is to measure critical rheological variables: pressure and volumetric flow rate, as these parameters reflect insight information into flow behavior. The consistency and quality of the entire process are related to the regulation of these variables. Furthermore, they serve as indicators of the viscoelastic material's properties during extrusion, particularly its viscosity. This knowledge of rheological variables also equips us with the ability to

classify materials, diagnose the extrusion process, and monitor material degradation. For instance, biomaterials are prone to degradation over time, which can result in potential failures during the printing process. This degradation becomes particularly noticeable through discernible changes in material characteristics, including variations in viscosity. For these reasons, it is essential to the extrusion device to have ability to monitor both pressure and volumetric flow rate.

To guarantee the high-quality output of LDM 3D printing, it is essential to maintain precise and intimate control over the rheological flow. This flow must be both smooth and accurate in order to successfully construct a 3D object. One crucial factor in line-based 3D printing is the control of linewidth. Achieving precision in linewidth needs the careful management of the volumetric flow rate. Given the inherent complexity and sensitivity of viscoelastic material rheology, controlling initial conditions is essential before the printing process. A common practice involves flushing a certain amount of material to clean the nozzle and prevent contamination. Additionally, it is crucial to regulate the pressure inside the nozzle, as it significantly impacts the rheological properties and ensures uniform residual stress within the viscoelastic material.

To enhance the LDM process, it is essential for the extrusion mechanism to possess the capability to both measure and regulate pressure and volumetric flow rate, as these factors are critical aspects of rheology. Employing a flexible mode actuation system allows for seamless transitions between regulating pressure and flow rate, ensuring precise control over initial conditions and resting of the printing process. However, it's important to acknowledge that LDM extruders are intentionally designed to be compact and lightweight, rendering them well-suited for attachment to the robot's end effector. To address this challenge, the proposed hardware has been designed to not only control these variables but also intrinsically sense them within the same mechanism, providing a comprehensive solution.

1.2 Objectives of the thesis

The objective of this project is to develop a flexible actuation system with intrinsic sensing for ram extrusion 3D printing. This system aims to enable both volumetric-controlled and pressure-controlled extrusion modes, providing flexibility for different stages of operation. It also allows real-time sensing rheology of the material.

CHULALONGKORN UNIVERSITY

1.3 Contributions to the field

This study explores the domain of Liquid-Deposition-Modeling (LDM) 3D printing. Such technology is highly suitable for printing bio matter which is heavily used in edible and medical industry. The central challenge of LDM is to the precise control of material flow. In response, we proposed an innovative actuation system that seamlessly transitions between pressure and volumetric control. Notably, we have also engineered the control algorithms tailored to each stage of the 3D printing process.

Moreover, we have introduced a real-time rheology analysis facilitated by an intrinsic sensing system that is embedded inside our actuation design. This capability allows for real-time assessment of material properties during the printing process. Beyond this, we have harnessed these rheological insights to implement an anomaly detection system. This innovation not only enhances the efficiency and flexibility of 3D printing but also substantially reduces material wastage throughout the process. These contributions significantly advance the capabilities and sustainability of additive manufacturing in these vital industries.

1.4 Scope of the thesis

To achieve the objective of this dissertation, the prototype is designed with an actuation that is able to switch the control to pressure and volumetric flow rate. Then the effectiveness of each control is analyzed and compared. After that, measurement by intrinsic sensing using the proposed actuation is evaluated.

จุฬาลงกรณ์มหาวิทยาลัย
CHULALONGKORN UNIVERSITY

1.4 Detailed Research Procedures

ขั้นตอน **Steps**	(เริ่มทำวิทยานิพนธ์เมื่อเดือน ……กันยายน 2022……) **(Month and Year theThesis Research Starts……September 2022……..)**	1	2	3	4	5	6	7	8	9	10	11	12	13	14	15	16	17	18
1	กำหนดหัวข้อและขอบเขตของวิทยานิพนธ์	↔																	
2	ศึกษาการควบคุมระบบขับแบบเคลื่อนที่ตามแนวเส้น		↔	↔	↔														
3	พัฒนา firmware สำหรับ prototype				↔	↔	↔	↔											
4	ศึกษาการทำวิจัย และไปดูงานที่ Kyushu Institution of Technology					↔	↔	↔	↔	↔	↔								
5	เก็บผลการทดลอง และ วิเคราะห์ผล											↔	↔	↔					
6	เขียนโครงร่างวิทยานิพนธ์												↔	↔					
7	เขียนวิทยานิพนธ์														↔	↔			
8																			

Research methodology

2.1 The conceptual design

In the context of Liquid-Deposition-Modeling (LDM) application, precise control of material flow is imperative to achieve accurate 3D printing outcomes. The rheological behavior of the material is primarily governed by two key factors: pressure and flow. Consequently, the extrusion system must effectively monitor and manage these two variables. The challenge of the system is to regulate flow across the domain of electric, mechanic and rheology. For instance, it is crucial to ensure the precision of the linewidth where intricately linked to the volumetric flow rate emanating from the nozzle. Simultaneously, understanding and controlling pressure are vital for comprehending the rheological properties within the syringe. The rise of resistive pressure encountered in the process may manifest as material clogs or material properties change within the nozzle. These issues can result in printing failures and hardware degradation. The goal of this system is to transfer the behavior of rheology to electrics domain through the mechanical transmission system. All elements through the dynamic chain are essential to have high visibility to ensure the fullness of the signal. Thus, the ram extruder in this context possesses the capability to both monitor and regulate pressure and volumetric flow.

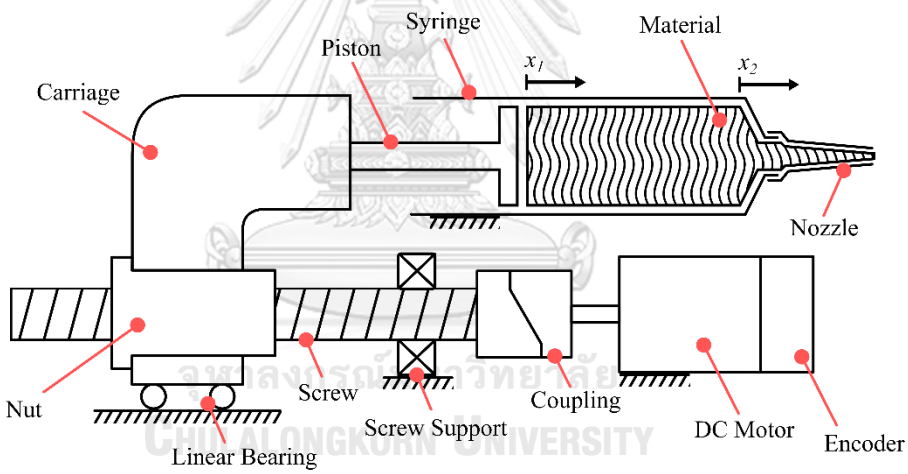

Figure 1 The conceptual design of the intrinsic sensing ram extruder with flexible control mode

The conceptual design of the proposed ram extruder with intrinsic sensing and switching mode actuation (Figure 1) consists of a motor driver, a permanent magnet DC motor, a ball screw, a syringe, and an extrusion material. Given the complexity of the extrusion application, the hardware encompasses various domains of physics. The system's input is a controllable voltage source, which serves as the motor driver. Once the motor is activated, electrical energy transforms into rotational energy, with voltage corresponding to angular velocity and current correlating with torque.

To enable the linear motion required for material extrusion, a mechanism capable of translating rotation into linear movement is necessary. A ball screw is one such mechanism, providing mechanical advantage by amplifying the maximum output force and enhancing the resolution of linear motion. However, the tradeoff for increased mechanical advantage in the

screw is reduced system visibility. The greater the mechanical advantage, the more it hinders the effect produced on the drive-side. Therefore, selecting the appropriate screw is critical for this project, as the sensing element is on the drive-side.

Once the translational motion is generated, the piston, firmly attached to the screw carriage, becomes controllable through the motor. By manipulating this piston, the system can regulate pressure and volume inside the syringe, which are directly linked to the flow of the extruded material. Pressure inside the syringe can be measured by monitoring the current flowing into the motor, while the extruded volume can be derived from the angular position of the motor's shaft.

The following section provides a detailed explanation of each element in the dynamic chain of the conceptual design.

2.2 Mathematics

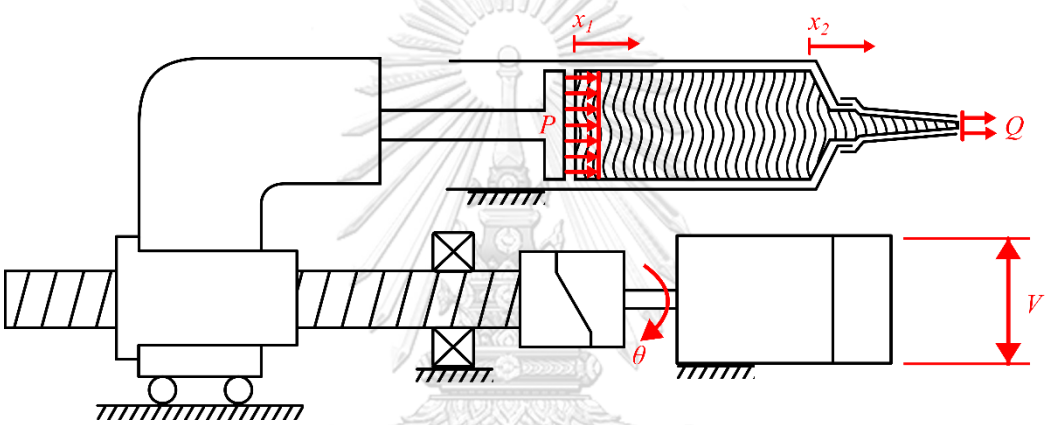

Figure 2 The schema of mathematics notation and the intrinsic sensing ram extruder with flexible control.

Considering the model of the proposed ram extruder, a controllable voltage source applies V voltage to a permanent magnet DC motor. The electric current, I, flows through an armature coil. If K_V is the speed constant and θ is the rotating angle of the shaft in rad, the equation of the motor is

$$V = L_m \frac{\partial}{\partial t} I + K_V \frac{\partial}{\partial t} \theta(t) + R_m I \qquad \textit{Eq. 1}$$

where R and L denote resistance and inductance, respectively. Torque, denoted by T, is then generated proportionally to I as

$$T = K_T I(t) \qquad \textit{Eq. 2}$$

where K_T is the torque constant of the motor.

With a rigid transmission with a flexible coupling, a feed position of plunger x_1 can be derived by the kinematic relationship of the ball screw:

$$x_1 = r\ tan(\alpha)\ \theta \qquad \textit{Eq. 3}$$

If α and r are the lead angle and radius of the screw, respectively.

Let μ be the coefficient of friction, then the angle of friction γ can be written as

$$\gamma = arctan(\mu) \qquad \textit{Eq. 4}$$

Thus, the equation of motion at carriage can be defined as

$$M\,r\ tan(\alpha+\gamma)\ \frac{\partial^2}{\partial t^2}\ x_1 + \frac{J\ \frac{\partial^2}{\partial t^2}\ x_1}{r\ tan(\alpha)} = T - F\,r\ tan(\alpha+\gamma) \qquad \textit{Eq. 5}$$

where M is the mass of the carriage, J is the moment of inertia, and F is the load of the screw. It is noted that γ can be varied by following the driving direction of the mechanism. Since extrusion only pushes the material through a nozzle, against the friction of flow. The model is assumed consistently forward driving. Thus, γ is always positive.

Next, consider the combined characteristics of viscous fluid and elastic solid that govern the behavior of the viscoelastic material. The important parameters defining these properties include elastic modulus which explains the elastic response of the material, and viscosity describes the viscous component.

The lumped element model is used to describe the print material. The elasticity is represented by a spring whose spring constant k corresponds to the elastic modulus of the material. By assuming a linear relation between flow resistance and flow rate, the viscous element could be modeled as a damper with a damping coefficient c corresponding to the viscosity. Assuming that the elastic behavior is dominated only in the syringe while only the viscous effect is mainly presented in the nozzle. And the small amount of extruded mass is neglected. The spring is connected to the damper in series, with a mass of the material that is inside the nozzle, m, attached between them.

CHULALONGKORN UNIVERSITY

The volumetric flow rate is assumed to be constant across the nozzle. Let the displacement of material that is entering the nozzle be x_2. The load that acts as a plunger can be defined by the spring effect inside the syringe as

$$F = f + k\,(x_1 - x_2) \qquad \textit{Eq. 6}$$

where f is overall friction which resists the system's motion. The equation of motion could then be derived as follows:

$$m\ \ddot{x}_2 = k\,(x_2 - x_1) - c(\dot{x}_2)\ \dot{x}_2 \qquad \textit{Eq. 7}$$

where $c(\dot{x}_2)$ is a non-linear damper that is a function of $\dot{x}_2$. If c_1 and c_2 are positive values, the $c(\dot{x}_2)$ can be defined as

$$c(\dot{x_2}) = c_1 + c_2 sgn(\dot{x_2})\dot{x_2} \qquad \textit{Eq. 8}$$

In the proposed design a permanent magnet DC motor, coupling, screw, and piston pump are connected in series, to drive the loaded material through the nozzle. Assuming that, two variables: θ and I, can be measured directly. With all the governing equations (Eq 1-7) presented, the design has an ability to sense and control both the pressure and volumetric flow rate.

Stability analysis: Lyapunov's second method of stability

Let X be a state vector of x_1, $\dot{x_1}$, x_2, $\dot{x_2}$ and I

$$X = \begin{bmatrix} x_1 \\ \dot{x_1} \\ x_2 \\ \dot{x_2} \\ I \end{bmatrix} \qquad \textit{Eq. 9}$$

A scalar function of state vector X, the Lyapunov candidate function Υ, is a function of total energy of the proposed ram extruder system. Such a function comprises of kinetic energy in screw and material flow, elasticity in material deformation, and electricity in inductor. The function can be defined as

$$\Upsilon(X) = \frac{k\,(x_1 - x_2)^2}{2} + \frac{L_m I^2}{2} + \frac{m_t\ \dot{x_1}^2}{2} + \frac{m\dot{x_2}^2}{2} \qquad \textit{Eq. 10}$$

where

$$m_t = \frac{M\ tan(\alpha+\gamma)\ tan(\alpha)\ r^2 + J}{r^2\ tan(\alpha+\gamma)\ tan(\alpha)} \qquad \textit{Eq. 11}$$

To ensure the properties of the Lyapunov candidate function Υ, the function has a stable point at X = 0

$$\Upsilon(0) = 0 \qquad \textit{Eq. 12}$$

From the Lyapunov candidate function of the system, each term has a square function multiplied by scalar. If all scalars have a positive value and $X \neq 0$, the summation of positive terms always be positive. Therefore, the rest state of X has a property of positive definition.

$$\Upsilon(X) > 0\ \ if\ \ X \neq 0 \qquad \textit{Eq. 13}$$

Considering the derivative of $\Upsilon(X)$ over time

$$\frac{d}{dt}\Upsilon(X) = J_t\,\ddot{x_1}\,\dot{x_1} + k\,(\,\dot{x_1} - \dot{x_2})\,(x_1 - x_2) + m\,\ddot{x_2}\,\dot{x_2} + L_m\,I\,\dot{I} \qquad \textit{Eq. 14}$$

Considering that the system with no voltage input V, Eq. 1 can be written as

$$0 = L_m \ \dot{I} + K_V \ \frac{\partial}{\partial t} \ \theta\,(t) + R_m \ I \qquad \textit{Eq. 15}$$

Substituting the derivative of Lyapunov candidate function (Eq. 14) by Eq. 2-3, 5-7, and 13 such a function can be written as

$$\dot{Y}(X) = -R_m I^2 - c(\dot{x_2})\,\dot{x_2}^{\,2} - f\dot{x_1} - \frac{K\,I\,\dot{x_1}}{r\ tan(\alpha)} + \frac{K\,I\,\dot{x_1}}{r\ tan(\alpha+\gamma)} \qquad \textit{Eq. 16}$$

The first term is trivially positive if R_m is a positive number.

Recall the sign function of any variable u

$$sgn(u) = \frac{u}{|u|} = \frac{|u|}{u} \qquad \textit{Eq. 17}$$

Considering the energy of non-linear damping term $c(\dot{x_2})\,\dot{x_2}^{\,2}$.

$$c(\dot{x_2})\,\dot{x_2}^{\,2} \ = \ (c_1 + c_2\ sgn\,(\dot{x_2})\,\dot{x_2}) \ \cdot \ \dot{x_2}^{\,2} \qquad \textit{Eq. 18}$$

Then,

$$c(\dot{x_2})\,\dot{x_2}^{\,2} \ = \ (c_1 + c_2\,\frac{\dot{x_2}}{|\dot{x_2}|}\,\dot{x_2}) \ \cdot \ \dot{x_2}^{\,2} \qquad \textit{Eq. 19}$$

and thus,

$$c(\dot{x_2})\,\dot{x_2}^{\,2} = c_1\dot{x_2}^{\,2} + c_2\frac{\dot{x_2}^{\,4}}{|\dot{x_2}|} \qquad \textit{Eq. 20}$$

Therefore, the energy of non-linear damping term is always positive in any $\dot{x_2}$ excluding zero.

The term of $f\dot{x_1}$ is always positive because the direction of friction f always resist the $\dot{x_1}$ motion thus

$$f = sgn(\dot{x_1})|f| = \frac{\dot{x_1}}{|\dot{x_1}|}|f| \qquad \textit{Eq. 21}$$

Then,

$$f\dot{x_1} = \frac{\dot{x_1}^{\,2}}{|\dot{x_1}|}|f| \qquad \textit{Eq. 22}$$

The fourth and fifth term can be transformed as

$$-\frac{K\,I\,\dot{x_1}}{r\ tan(\alpha)} + \frac{K\,I\,\dot{x_1}}{r\ tan(\alpha+\gamma)} \ = \ \frac{K\,I\,\dot{x_1}}{r} \cdot \left(\frac{tan(\alpha) - tan(\alpha+\gamma)}{tan(\alpha)\,tan(\alpha+\gamma)}\right) \qquad \textit{Eq. 23}$$

The key challenge of Eq. 23 is γ can be written as

$$\gamma = \begin{cases} -\gamma_{abs} & ; backward\ driving \\ \gamma_{abs} & ; forward\ driving \end{cases} \qquad Eq.\ 24$$

where γ_{abs} is an absolute value of friction angle. This term affects the sign of Eq. 23. The sign of γ depends on direction of driving of the screw. As the energy flow through screw forwardly, meaning that the screw drive system, the screw is forward driving. If the energy is flow from output-side to input-side, the screw is in backward driving. Since, $K\,I\,\dot{x_1}$ is representative of rotation motion's power. As the screw move forward such term is positive, conversely, the term is negative when backward drive.

$$\gamma = \begin{cases} -\gamma_{abs} & ; K\,I\,\dot{x_1} < 0 \\ \gamma_{abs} & ; K\,I\,\dot{x_1} > 0 \end{cases} \qquad Eq.\ 25$$

In case of $K\,I\,\dot{x_1} < 0$

$$\left(\frac{tan(\alpha) - tan(\alpha - \gamma_{abs})}{tan(\alpha)\,tan(\alpha - \gamma_{abs})}\right) > 0 \qquad Eq.\ 26$$

And when $K\,I\,\dot{x_1} > 0$,

$$\left(\frac{tan(\alpha) - tan(\alpha + \gamma_{abs})}{tan(\alpha)\,tan(\alpha + \gamma_{abs})}\right) < 0 \qquad Eq.\ 27$$

Thus, we can conclude that the summation of

$$-\frac{K\,I\,\dot{x_1}}{r\ tan(\alpha)} + \frac{K\,I\,\dot{x_1}}{r\ tan(\alpha + \gamma)} < 0 \qquad Eq.\ 28$$

Overall, every term in Eq. 16 can be concluded that their summation produces negative number, thus the system in all $X \in \mathbb{R}^5\ and\ \neq\ 0$ can be concluded to be

$$\dot{Y}(X) < 0 \qquad Eq.\ 29$$

Thus, we can conclude that the system has a property of asymptotic stability.

The measurement and regulation of pressure

The force from material elastic deformation, $k\,(x_1 - x_2)$, is the analogous representative of pressure force inside piston. If it assumes that the pressure equally distributes inside the piston, the pressure P then can be derived as

$$P = 4 \cdot \frac{k\,(x_1 - x_2)}{\pi\,D^2} \qquad Eq.\ 30$$

where the piston has a circular cross-section area and D is the diameter of piston.

Combining Eq 2, 3, 5, 6, and 8, the pressure P can be derived from measurement of current I and the angular position θ following:

$$P = \frac{4\left(K_T\, I - (M\ tan(\alpha+\gamma)\ tan(\alpha)\ r^2\ + J\,)\frac{\partial^2}{\partial t^2}\ \theta - f\ tan(\alpha+\gamma)\ r\right)}{D^2\, r\, \pi\ tan(\alpha+\gamma)} \qquad \textit{Eq. 31}$$

If the second-order derivatives of θ can be obtained and the friction f is priorly known. In summary, Eq. 31 illustrates that the pressure can monitoring real-time with only the use of position and current sensor.

If the system converges to a steady state, the acceleration is equal to zero and the current remains constant. Substituting Eq. 30 to Eq. 31, pressure P then can be regulated by voltage V.

$$P = -\frac{4\left(f\, r\ tan(\alpha+\gamma) - \dfrac{K_T\left(V(t) - K_V\ \dfrac{\partial}{\partial t}\ \theta(t)\right)}{R_m}\right)}{D^2\, r\, \pi\ tan(\alpha+\gamma)} \qquad \textit{Eq. 32}$$

Eq. 32 shows capabilities of the pressure regulation by controlling the voltage source V. The equation is seen to affect by the disturbance of back-EMF. Such a disturbance is a function of θ that also can be measured. With this availability, the machine can compensate the back-EMF effect by measuring the angular speed of motor.

The measurement and regulation of volumetric flow rate

The volumetric flow rate of the material, Q, is proportional to the second differentiation of x_2 over time with the multiplication of area of piston.

$$Q = \frac{\pi\, D^2\ \dfrac{\partial}{\partial t}\ x_2(t)}{4} \qquad \textit{Eq. 33}$$

The elastic behavior of the material is fully deformation at the steady state, meaning that the rate of change for x_1 and x_2 are coupled. Thus, it can then be derived from the differentiation over time of θ, via Eq 3. By applying the close-loop controller over the measured θ, the steady state volumetric flow rate, Q, can be directly handled.

$$Q = \frac{\pi\, D^2\, r\ tan(\alpha)\ \dfrac{\partial}{\partial t}\ \theta(t)}{4} \qquad \textit{Eq. 34}$$

The assessment of the rheological properties

Considering the rheology of material that represents as damping coefficients, the material viscous force displays how difficult it is to keep material flow. This coefficient can discriminate various materials that have different extrudability. This knowledge of rheological properties can be determined the material-health and material-clogging. Such benefit can improve the success rate in 3D printing.

จุฬาลงกรณ์มหาวิทยาลัย
CHULALONGKORN UNIVERSITY

If the proposed design can measure current I and angular position θ and then friction f can be modeled and priorly known via calibration. In the steady state, damping coefficient can be calculated by combining the Eq 1-7 as

$$c(\dot{x_2}) = \frac{K_T\, I(t) - f\, r\ tan(\alpha + \gamma)}{r^2\ tan(\alpha + \gamma)\ tan(\alpha)\ \frac{\partial}{\partial t}\ \theta(t)} \qquad \textit{Eq. 35}$$

2.3 Simulation

The simulation of the research plant is created using MATLAB Simscape framework. Such an approach, using the concept of bond graph, models the relationship among physical element with energy channels. Within this framework, the electrical domain is depicted in blue, while the mechanical rotational and translational domains are respectively represented in light-green and dark green. The connections between these components symbolize energy flow pathways, allowing energy to move in all directions. Consequently, this model can be applied with various scenarios within a single simulation model. Moreover, the program built an abstract layer in which detailed parameters are concealed inside each component. The solver engine is hide in the background lower layer which provide a better focus and flexibility on how physical components are interacting with each other.

The components that used in the model are

- Controlled voltage source
- Rotational Electromechanical converter
- Resistor
- Inductor
- Electrical reference
- Mechanical rotational reference
- Lead screw
- Translational friction
- Translational spring
- Mass
- Nonlinear translational damper
- Mechanical translational reference
- Current sensor
- Ideal rotational motion sensor

Controlled voltage source

Figure 3 Simscape block: Controlled voltage source

จุฬาลงกรณ์มหาวิทยาลัย
Chulalongkorn University

The Controlled Voltage Source block symbolizes an ideal voltage source capable of sustaining a constant output voltage irrespective of the current flowing through it. The output voltage, denoted as V, equals the numerical value Vs provided at the physical signal port.

Rotational Electromechanical converter

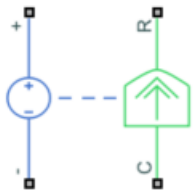

Figure 4 Simscape block: Rotational Electromechanical converter

Rotational Electromechanical Converter serves as a bridge between the electrical and mechanical rotational realms. When considering the current (I) and voltage (V) across the electrical ports, as well as the torque (T) and angular speed (w) across the mechanical ports, the following relationships hold:T=K·I, V=K·w. Here, the parameter K signifies the constant of proportionality, with unit's equivalent to Nm/A or V/(rad/s). The torque and back emf equations sharing the same K value depict a lossless electromechanical energy conversion.

If the electrical current I flows from the positive to negative ports, a positive torque results, acting from the mechanical C to R ports. This direction can be reversed by utilizing a negative value for K.

Resistor

Figure 5 Simscape block: Resistor

The voltage-current relationship for a linear resistor is expressed as V=I*R, where R stands for the constant resistance measured in ohms.

According to convention, the voltage across the resistor is determined by $V_+ - V_-$, and the current is considered positive when it flows from the positive to the negative terminal. This convention guarantees that the power absorbed by a resistor remains positive.

Inductor

Figure 6 Simscape block: Inductor

This block is the modeling of a linear inductor. It defines the relationship between voltage (V) and current (I) as V=LdI/dt, where L represents the inductance measured in Henries (H).

The presence of Series resistance and Parallel conductance accounts for minor parasitic effects. The series resistance is utilized to depict the DC winding resistance or resistance arising from the skin effect. Additionally, a small parallel conductance might be necessary for simulating certain circuit topologies. Further details can be found in the documentation.

Electrical reference

Figure 7 Simscape block: Electrical reference

This block acts similar to electrical ground. A Simscape model must contain at least one of this blocks.

Mechanical rotational reference

Figure 8 Simscape block: Mechanial rotational reference

This block represents a mechanical rotational reference point, that is, a frame or a ground. Use it to connect mechanical rotational ports that are rigidly fixed to the frame(ground).

Lead screw

Figure 9 Simscape block: Lead screw

Such block represents a lead screw that converts rotational motion into translational motion and vice versa. It can be optionally included friction losses specified either in terms of the friction coefficient and geometrical parameters, or in terms of efficiencies for forward (from screw to nut) and backward (from nut to screw) power flows. If efficiency for reverse power flow is set to a negative value, the mechanism exhibits so-called self-locking features, and power can not be transmitted from nut to screw unless some torque is applied to the screw to release the locked mechanism.

Translational friction

Figure 10 Simscape block: Translational friction

จุฬาลงกรณ์มหาวิทยาลัย
Chulalongkorn University

The block represents friction in the contact between moving bodies. The friction force is simulated as a function of relative velocity and assumed to be the sum of Stribeck, Coulomb, and viscous friction. The sum of the Coulomb and Stribeck frictions at zero velocity often referred to as the breakaway force.

Translational spring

Figure 11 Simscape block: Translational spring

The block represents an ideal mechanical linear spring. The force (F) and motion (x) in this block follows F = Kx, where K is a stiffness of the spring.

Mass

Figure 12 Simscape block: Mass

The mass block represents an ideal mechanical translational mass that is described with the following equation: F = m*dv/dt where F is force, m is mass, v is velocity of the mass, and t is time.

Nonlinear translational damper

Figure 13 Simscape block: Nonlinear translational damper

The Nonlinear Translational Damper block represents a nonlinear translational damper. Polynomial and table lookup parameterizations define the nonlinear relationship between damping force and relative linear velocity. The damping force can be symmetric or asymmetric about the zero velocity point. The block applies equal and opposite damping forces on the two translational conserving ports.

The symmetric polynomial parameterization defines the damping force for both positive and negative relative velocities according to the expression:

$$F=b_1v+sign(v)\cdot b_2v^2+b_3v^3+sign(v)\cdot b_4v^4+b_5v^5$$

Mechanical translational reference

Figure 14 Simscape block: Mechanical translational reference

This block represents a mechanical translational reference point, that is, a frame or a ground. Use this block to connect mechanical translation ports that are rigidly fixed to the frame(ground).

Current sensor

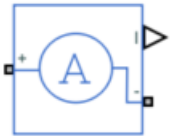

Figure 15 Simscape block: Current sensor

The block represents an ideal current sensor, that is, a device that converts current measured in any electrical branch into a physical signal proportional to the current.

Ideal rotational motion sensor

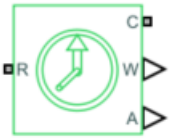

Figure 16 Simscape block: Ideal rotational motion sensor

จุฬาลงกรณ์มหาวิทยาลัย
CHULALONGKORN UNIVERSITY

This block can measure angular velocity or angle in a mechanical rotational network. The sensor is ideal since it does not account for inertia, friction, delays, and energy consumption.

Solver

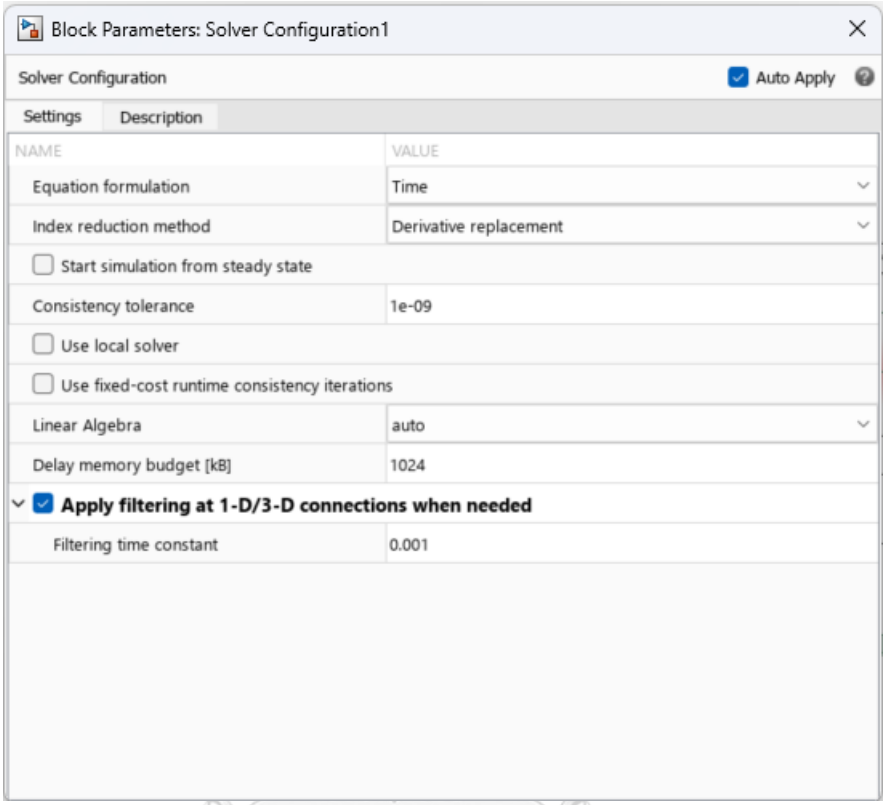

Figure 17 Solver setting of Simscape model

จุฬาลงกรณ์มหาวิทยาลัย

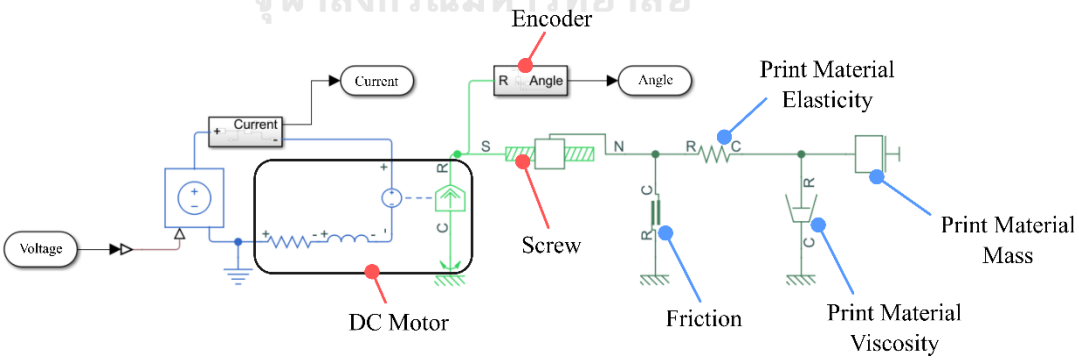

Figure 18 The MATLAB Simscape model of the proposed design

Figure 18 is a model of the proposed system that associated with above equation (Eq 1-7). The input is a controllable voltage source that drives a DC motor. The DC motor contains a resistor, inductor, and electrical-rotational converter. The converter transfers current to torque and angular speed to back electro-motive-force. The screw element transfers the rotational to translational motion. The resistive force, such friction and elasticity of fluid are attached to carriage port. In the other end of spring element (Print material elasticity), the motion is

connected with print material mass and viscosity. This node represents the motion of material that flows through a nozzle.

The measurement of damping coefficient is examined within the simulation model. The input voltage is applied at various constant levels of 8, 10, and 12 V. The parameters of the model can be found in Table *1*. The damping coefficient is varied between 0 to 10,000 Ns/m (incremented with 1000 Ns/m). The current and speed of the motor are obtained to predict the damping coefficient of the loaded material. In the simulation, the friction is already known however assumed to be imprecisely modeled within 5% error. The estimation of the damping coefficient is conducted by using Eq. 35.

จุฬาลงกรณ์มหาวิทยาลัย
CHULALONGKORN UNIVERSITY

Table 1 The parameters of the Simscape model

Symbols	Values	Unit	Description
R_m	4	Ω	Motor Resistance
L_m	99.5	μH	Motor Inductance
K_V	0.0261	V·s/rad	Motor Speed Constant
K_T	0.0261	N·m/A	Motor Torque Constant
J	0.001	kg·m^2	System Moment Inertia
f	30	N	System Friction
r	0.004	m	Screw Radius
α	4.55	N/A	Lead Angle
μ	0.05	kg	Screw Friction Coefficient
D	0.016	m	Diameter of Piston
M	0.01	kg	Carriage Mass
m	0.1	kg	Material Mass
k	100,000	kN/m	Material Spring Constant
c_1	1-10,000	N·s/m	First order Damping Constant
c_2	0	N·s/m	Second order Damping Constant

Table 2 The variable of the Simscape model

Symbols	Unit	Description
x_1	m	Displacement of plunger
x_2	m	Displacement of Material Entering the Nozzle
θ	rad	Rotation Angle of Screw
V	V	Voltage
I	A	Current
T	N m	Motor's Torque
F	N	Screw Load
P	Pa	Pressure
Q	m^3/s	Volumetric Flow Rate

จุฬาลงกรณ์มหาวิทยาลัย
CHULALONGKORN UNIVERSITY

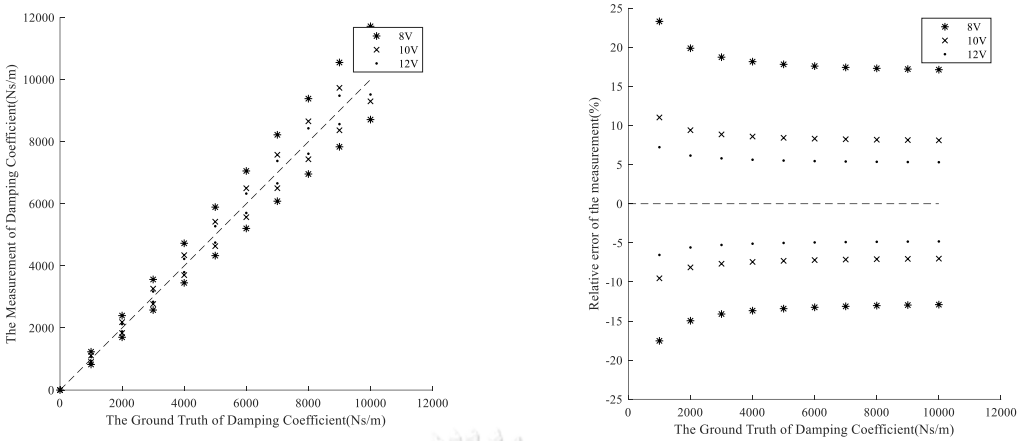

(a) (b)

Figure 19 The simulation result of the damping coefficient measurement (a) and relative error of the measurement (b).

Figure 4 displays the results of damping coefficient measurements in a Simscape simulation. Current and speed values are obtained at the end step of each simulation, which steady-state condition holds true. The dashed line, inclined at a 45-degree angle, represents the precise prediction where true values align with the measured values. Evidently, the measurements closely correlate with the input damping coefficient, with data points closely following the reference line. Nevertheless, a 5% friction error introduces disruptions in the measurements, leading to deviations from the 45-degree line of prediction. Significantly, the magnitude of the true damping coefficient substantially affects prediction errors. The most pronounced relative error (23.31%) emerges when the damping coefficient is 1000 N·s/m, and the input voltage is 8 V. Notably, friction perturbations escalate the measurement error from 5% to 23.31%. The trend of the relative error decreases and eventually converges as the true damping coefficient increases. For instance, with an 8V voltage input, the error converges to around -12% and 17%. It's essential to note that the error is asymmetric; when friction exceeds expected values, speed decreases. According to prediction equation Eq. 12, speed is in the denominator, causing a non-linear error effect, resulting in this asymmetry. To minimize fluctuations, the results suggest that using a higher voltage is advisable, leading to reduced error. In summary, the results demonstrate the capability of the proposed design to intrinsically sense the rheological properties of the flow by monitoring current and rotational angle.

2.4 Hardware Implementation

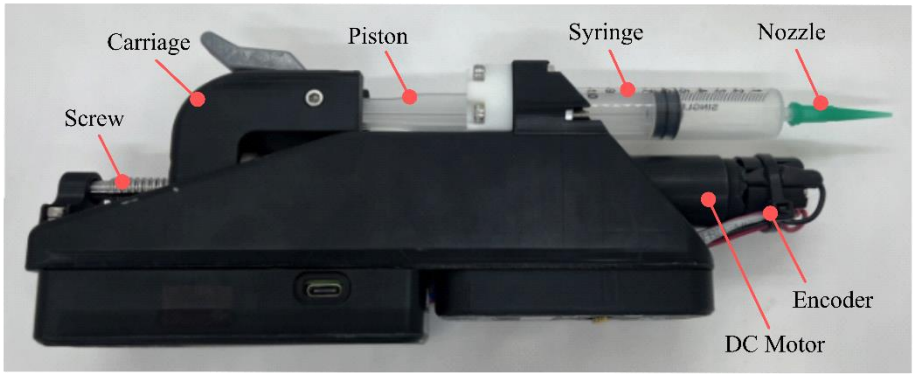

Figure 20 The actual implementation of an intrinsic sensing ram extruder with flexible control for liquid deposition modeling 3d printing

The custom 3D printer nozzle assembly (depicted in Figure 20) is constructed based on the proposed idea. We have chosen the Faulhaber DC motor model 2342S024CR, along with an incremental encoder IE3-1024 L, to serve as the primary actuator. It is linked to the THK ball screw BNK0802 using a flexible coupling. The frame and various passive components of the extruder are produced through 3D printing using resin. This design allows for the secure attachment of a 10mL syringe main body to the frame, with the syringe piston motion being synchronized with the ball screw nut.

To manage the hardware of the extruder, we employ a specially designed PCB. This PCB incorporates the DRV8876PWPR DC motor driver chip, known for its capability to sense electrical current, thus facilitating real-time monitoring of the current supplied to the motor. The control of the extruder is carried out by an STM32-based MCU (main-controller-unit), which is responsible for handling communication and signal processing. Its firmware is programmed to switch between a constant voltage mode (pressure-controlled) and a closed-loop mode (volumetric-controlled) upon receiving specific G-CODE commands. In the closed-loop mode, a proportional-derivative controller is employed to precisely control the motion of the motor. Over time, the MCU collects data on motor position and electrical current for use in experiments. The dimensions of the assembly, excluding the syringe, measure approximately 220x110x50 mm, and it weighs 622 grams.

This printhead is designed to interface and communicate with mainstream 3D printers through a specially tailored adapter. The adapter transmits the STEP/DIR signals typically used for stepper-based extruders in typical Fused Deposition Modeling (FDM) printers. In the closed-loop extrusion mode, this custom extruder receives these signals from the printer and regulates the extrusion rate based on the STEP signal. Additionally, the adapter relays serial communication for the extruder, enabling the use of specialized G-CODE commands and the logging of extruder data, including piston position and electrical current.

Pressure extrusion

3.1 Pressure measurement

Pressure observer

Recall Eq. 31, pressure inside material can be derived from the measurement of current and angular acceleration of a dc motor. To be more precise, armature current flows through the motor, generates torque, and then drives a piston forwardly. Consequently, the carriage and piston accelerates. The piston then presses the material, generates pressure, and forces material to flow. However material resist to flow because of viscosity. Furthermore, the mechanism has a friction which resist the motion which reduces the effort to drive the material through. Thus, the relationship of pressure is an amout of current reduces by the friction and some portion that generate system momentum.

From the relationship that can be seen in Eq. 31, we can assume that the amount of accelaration can be neglected as the system usually operate in steady state. The operation of LDM extrusion commonly generates steady flow which have constant velocity. Additionaly, the angular acceleration that derived from position has poor signal-to-noise ratio. Since the signal is assessed by second derivative of measurement, the derivative noise is amplified by square. Thus, the pressure observer is built by the measurement of current and neglect the accelaration. The observer can be written in mathematic form in linear equation as

$$P = A_1 I + A_2 \qquad \textit{Eq. 36}$$

Pressure sensor

For conducting the experiment, the pressure sensor is needed for calibrating and validating the observer and controller. The pressure that was selected for this experiment is an amplified basic pressure sensor from Honeywell. The sensor is Honeywell ABP150PGSA3. The mechanism is based on piezoresistive effect which offers sensing device for the pressure. The minimum and maximum pressure input is 0 and 150 psi or about 10.34 bar, respectively. The output signal is a digital signal: SPI with the maximum bit rate of 800 kHz and response time of 0.46 ms. The resolution of the sensor is 12 bits which is equal to 0.0025 bar. The sensor's accuracy is 0.026 bar.

Table 3 the characteristics of selected pressure sensor

ABP150PGSA3	
Operating voltage	3V
Operating range	0 – 150 psi
Output	SPI (800 kHz)
Response time	0.46 ms
Resolution	0.0366 psi
Accuracy	0.375 psi

Parameter acquisition

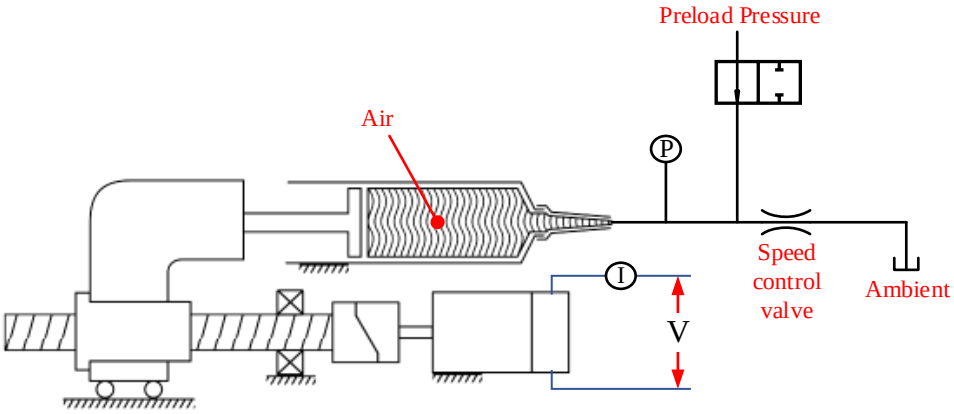

(a)

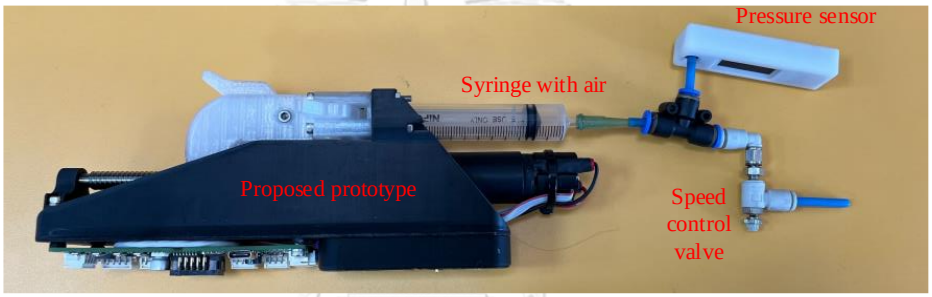

(b)

Figure 21 (a) Diagram of pressure measurement. The setup comprises a proposed machine, pressure sensor, valve, speed control valve, and preload pressure. (b) The actual setup of the experiment.

From Eq. 36, the pressure observer needs to fill A_1 and A_2. These parameters are a function of the machine, e.g., cross section area inside syringe, motor characteristics and friction. To assess such parameters, the actual experiment is performed. The experiment uses a pressure sensor (Honeywell ABP150PGSA3) to collect actual pressure while the system operates. The actual pressure was brought to compare with current to fit the parameters by Eq. 36.

In Figure 21, the experiment was conducted by installing pneumatic tubes on the nozzle. The tube was sealed so the fluid was trapped inside. The air was selected to be the sample material. The tube was connected to a pressure sensor and then a three-way-junction that connects to solenoid valve and preload pressure source, and the speed control valve. The role of speed control valve is to represent the flow resistance of viscoelastic material. This valve reduces the flow thus the pressure inside the system can be built up. Noted that, the valve allows fluid to leak which is suitable for represent the extrusion of material. The preload pressure component is important for create an experiment on high pressure. To build pressure, the volume of fluid container must be decreased. The decreased volume is inverse to fluid pressure. Thus, to get high pressure, preload pressure is fit to adjust the pressure of starting point to make the system work in operating range of lead screw motion.

The proposed system was commanded by serial communication which connected to a computer. The pressure sensor was communicated with STM32 micro-controller then

transmitted data to a computer by serial port. These two devices were handled by a single process python program with multi-threading. The data was collected with a rate of about 500 Hz. The proposed machine was commanded with constant voltage at 40%, 50%, 60%, and 70% of maximum voltage (12V). The data was collected and then excluded the transient response.

Effectiveness of pressure measurement

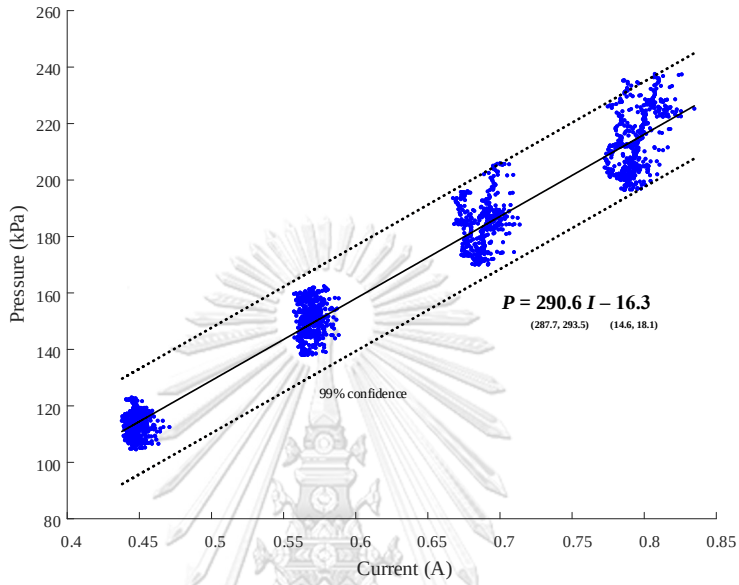

Figure 22 The graph of actual experiment of proposed machine extrusion with constant voltage (40%, 50%, 60%, and 70% of 12V). The sample material that is used is the air. The data shows a linear relationship between current and pressure.

From Figure 22, the graph shows correlation between the pressure and current. The data shows four clusters of data point which link to the four levels of commanded voltage. The clusters can represent linear relationships which associated with Eq. 31 when the acceleration term was neglected. Noted that, in this experiment the data only in steady state is included. Thus, the system tends to move with constant speed. Increase in current gives rises to pressure data. This is because more torque is generated due to current. Thus, more force is driven to the piston and generates more pressure. This linear trend can also be used to fit the observer function in Eq. 36 ($A_1 = 290.6\,\text{kPa/A}$, $A_2 = -16.3\,kPa$). From this experiment, the measurement of pressure by proposed observer has a sensitivity of 290.6 kPa/A. From this current hardware which has a current sense module with 12-bit resolution for 3.3 A, the resolution of pressure sensing is 0.23 kPa. Friction of whole system is represented in pressure loss form of 16.3 kPa in A_2 parameter.

This pressure observer can be used with other material beside the sample material (air). From Eq. 31, there is no effect of material properties (spring and damping coefficient). However, the observer is built upon the neglection of acceleration thus the limitation is the correctness of the steady state assumption. The material that has higher viscous makes the system respond slower. Such material favors the observer which reduces the effect of acceleration term. The presence of A_2 parameters show the effect of friction. The friction affects the system in terms of the accuracy of measurement which offset the measure value with constant amount. Thus,

the observer can be well precise as if the friction amount is deterministic and known. This friction can be predetermined with calibration similar to this experiment.

In summary, the observer is constructed with Eq. 36 and then determined the parameters by conducting the experiment. The result shows the sensitivity of measurement with 290.6 kPa/A and resolution of proposed design is 0.23 kPa.

3.2 Pressure control

According to the previous section, the relationship between current and pressure is stated. This gives opportunities for controlling the pressure inside the syringe by regulating the amount of current flow to the motor. Thus, it is needed to build current control.

Current control

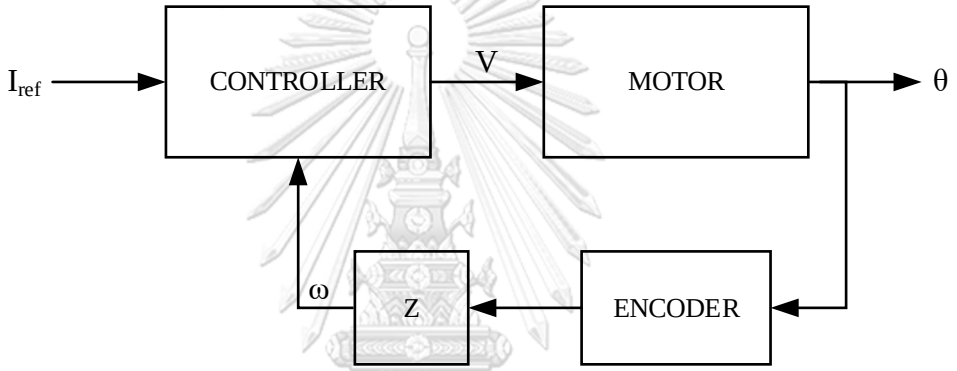

Figure 23 The schema of current control for a dc motor.

From motor equation (Eq. 1), voltage V has a combination of resistance times current, inductance times time-derivative of current and the back-EMF term. Due to the dc motor in proposed design is coreless motor. The inductance inside motor is relatively low thus, the inductive term is neglected. The current inside motor can be written as

$$I = \frac{V - K_b\omega}{R} \qquad \textit{Eq. 37}$$

This equation shows the effect of motor speed which can reduce the current that flows through the motor with some given level of drives voltage. This equation also shows the point that back-EMF is equal to input voltage which current does not flow. In this point, there is no torque since current is zero. The motor does not accelerate so this points the motor has a maximum speed. Also, this equation shows the highest current and torque is when motor has a zero speed (stall).

To control the current, the controller needs to compensate for the back-EMF term. Thus, the assessment of angular speed can be sufficient for constructing the current control by knowing the back-EMF coefficients and resistance of the motor. The controller can be built with

$$V = K_R\, I_{ref} + K_{b,predicted}\, \omega \qquad \textit{Eq. 38}$$

Then substitute I_{ref} with Eq. 37, gives

$$V = K_R \frac{V_{ref} - K_b \omega}{R} + K_{b,predicted}\, \omega \qquad \textit{Eq. 39}$$

If gain K_R is equal to R and $K_{b,predicted}$ is equal to K_b, current then algebraically equal to voltage V.

However, the lack of angular speed measurement resulted in need of derivative of angular measurement. This gives poor resolution of angular speed observation from the derivative noise. Lowpass filter may need for reduce the effect of derivative noise.

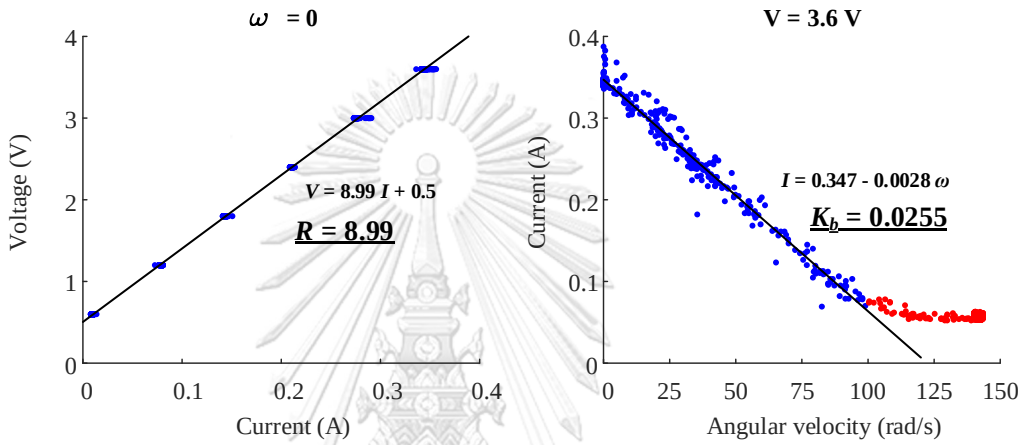

Figure 24 The result of motor characteristics acquisition. The graph on the left shows correlation between current and voltage at zero angular speed which gives slope of the graph equal to resistance of the motor (8.99 ohm). The graph on the right shows relationship of angular speed and current which can indicate the speed constant of the motor (0.0255 V/(rad/s)).

From Eq. 1, when the motor is not rotated, angular speed is equal to zeros. If the inductance can be neglected, then the equation can be written as,

$$V = I\,R \qquad \textit{Eq. 40}$$

This equation shows that the slope between current and voltage is equal to resistance inside the motor.

From Eq. 40, The experiment was set up on the uninstalled motor that was used in the proposed prototype. The rotor of the motor was fixed to the ground and unable to rotate. The difference voltage level was applied to the motor. Then current and torque are created. The current was measured by current sense unit inside the motor controller of proposed prototype. The data was collected at 1000 Hz via serial communication.

From Figure 24 (left), the graph shows linear trend between current and voltage which highly correlated with Eq. 40. The data point shows six clusters associated with the six levels of commanded voltage. The slope which represents the resistance is equal to 8.99 Ohm. The graphs show an offset from zero about 0.5 V. Such an effect can occur by non-linearity of the

electronic circuit. However, the experiment evident the precise result of resistance at 8.99 Ohm because of goodness of linearity.

To acquire motor speed constant, Eq. 39 has been used. The experiment was created on constant voltage level at 3.6 V. The rotor shaft was applied with varied torque resistance to simulate variable angular speed. Then the data was collected in a similar way to the previous test.

From Figure 24 (right), the graph demonstrates linear line until 100 rad/s. The graphs then gradually convert to zero-slope. From theoretical equation (Eq. 39), the red data points were excluded because of non-linear effect that not being used in operating point. Thus, only the blue data points were considered to fit to Eq. 39. The graph shows linear trend where the current is equal to 0.347 – 0.0028 ω A where the slope is negative. Such trend reflects the resultant of back-EMF where the current is reduced due to accumulated speed of rotor. After acquiring the resistance of the motor, the motor speed constant can be derived by Eq. 39 which equal to 0.0255 V/(rad/s).

Overall, the current control is constructed by modeling a dc motor system, designing the current controller, then acquire all parameters, and finally, apply all parameters to the controller. The K_R , equal to resistance of the motor, is 8.99 and $K_{b,predicted}$, equal to speed constant of the motor, is 0.0255.

Pressure control

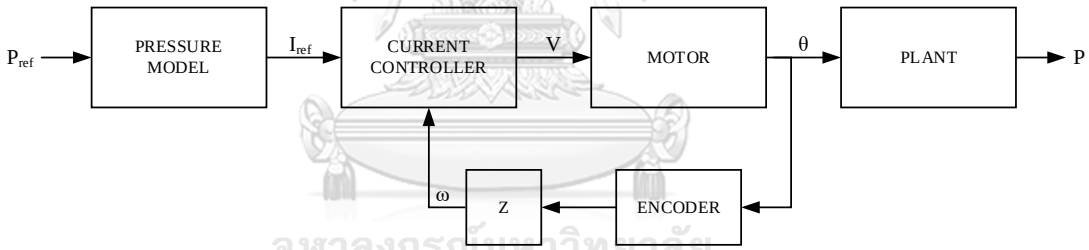

Figure 25 The schema of pressure control.

After finishing of current controller and acquisition of relationship between current and pressure, the pressure model can be used for building the controller to regulate pressure in material. The amount of pressure can derive to form current reference that feed to current controller. Then the level of voltage can be adjusted based on velocity that observed from an encoder.

The evaluation of pressure control was performed by the set up similar to combination in Figure 21. The proposed system was commanded by serial communication which connected to a computer. The proposed machine was commanded with constant voltage at 40%, 50%, 60%, and 70% of maximum voltage (12V). Then the machine pushes the air until it hit the limit switch which installed at maximum position of screw axis.

Effectiveness of pressure control

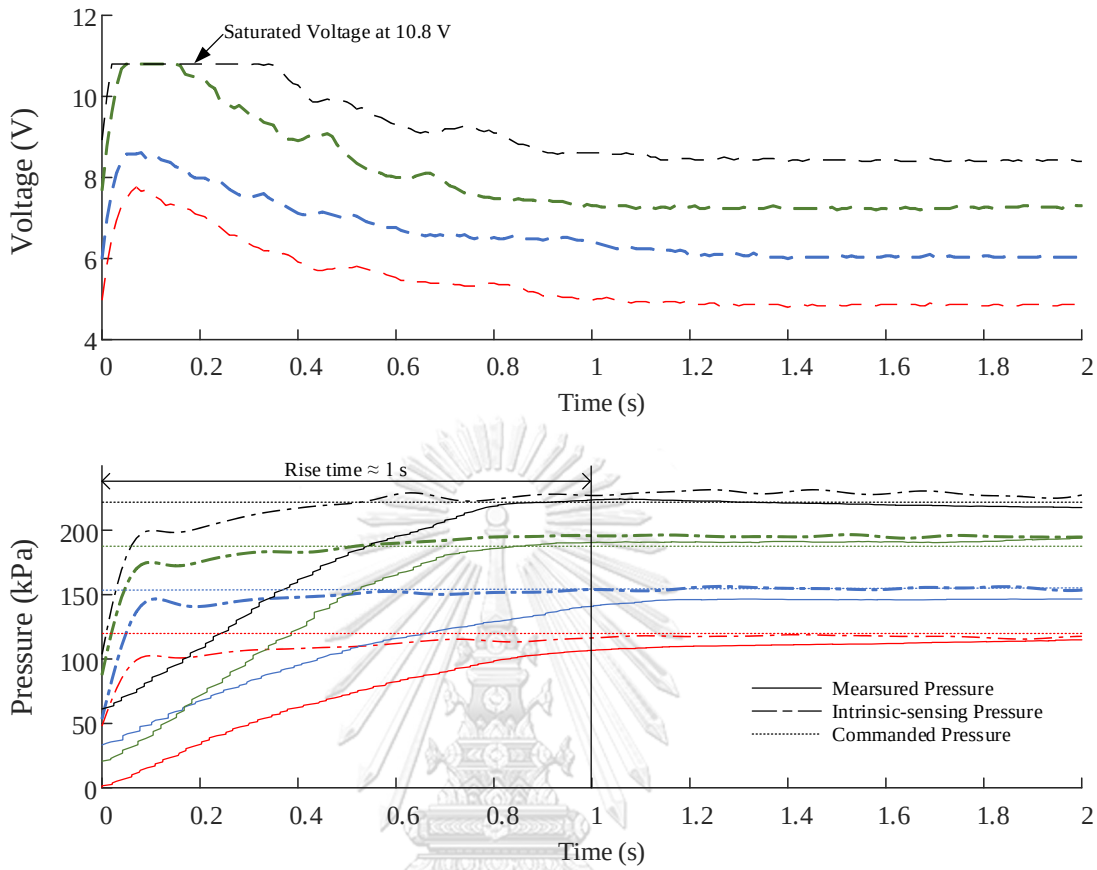

Figure 26 The graph of pressure control performance. The upper graph shows the voltage of motor from controller command. The lower graph shows measured pressure, derived pressure (from current), and pressure reference.

From Figure 26 (lower), the graph shows performance of pressure control. The experiment was done by four different levels of pressure reference (120, 154, 188, and 222 kPa). The response gradually converts to steady state at end of rise time (about 1 s). The pressure signal from sensor tends to follow the pressure reference. This evidence shows that the proposed method to control the pressure is effective. However, there are some errors which occurred from defect of the mechanism. For example, friction which can be varied by position and time, causing the disturbance in pressure control. A higher amount of friction reduces the force that presses material then the pressure is decreased. The performance of sensing pressure by the current is also shown in the graph. In the period before rise time elapsed, the signal exhibited poor accuracy due to the system acceleration. This can be seen by large deviation from the signal of pressure sensor. However, after reaching steady state, the pressure signal from current sense shows good accuracy with below 15 kPa error (1.5 – 2 s).

Upper graph in Figure 26 shows the response of input voltage due to the current controller after the pressure reference is given. The response reaches a steady state at rise time (1 s). The trends show peak at around the starting point where the system has velocity. The controller needs to compensate the back-EMF by increasing the amount of voltage to maintain the current level. At starting point, the system is in rest, thus the voltage level is equal to current

times resistance. After that the system accelerates from current flows, the velocity is accumulated, and then voltage rises. Finally, the air inside the syringe is pressed enough so that the pressure can resist the motion. As a result, the system is back to equilibrium where the torque from motor is equal to the viscosity of the air that needs to leak of the speed control valve. The system is very slow so that the effect of back-EMF can be seen neglected. The voltage level is reverted to around the level at t=0. It is good to note that the ceiling bound of 188 and 222 kPa pressure reference (green and blue) at about 0.2 s is a saturated voltage at 90% of 12V (supply voltage).

In conclusion, the performance of pressure and current control are demonstrated. The pressure controller gives the rise time of 1 s for air as sample material. The pressure controller has favorable accuracy at below 15 kPa error. The pressure observer that built by current sense has a promising result in steady state however poor result exhibit in transient state due to the acceleration.

จุฬาลงกรณ์มหาวิทยาลัย
CHULALONGKORN UNIVERSITY

Volumetric flow extrusion

4.1 Volumetric measurement

Recall to Eq. 33,

$$Q = \frac{\pi D^2 \frac{\partial}{\partial t} x_2(t)}{4} \qquad \textit{Eq. 41}$$

where x_2 is a displacement of material in a syringe. The displacement of piston x_1 can control the volume inside the syringe. If the piston pushes forward, the volume then decreases. Consequently, the material inside is compressed. The compressibility varies depending on the type of viscoelastic material. It is good to note that when the material size is reduced, material has a negative strain that is associated with a stress. The stress inside material is a pressure.

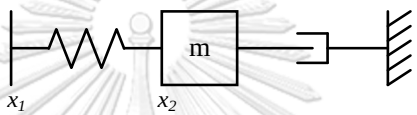

Figure 27 The analogy for material extrusion mechanism by syringe extrusion based on Maxwell model. The position of piston is denoted by v and the position of material is denoted by x_2.

From Figure 27, viscoelastic material can be modeled by Maxwell model. The complex modulus of viscoelasticity comprises of storage modulus and loss modulus. The storage modulus is represented by spring where the energy is stored when the material is deformed. When the stress is relieved, the material can be restored to the original shape like spring and is reverted to the original position. Besides, the energy that flows through the loss modulus is completely lost. Such an element is modeled by damping element. When the material is deformed, it cannot restore to its original state.

In a syringe, there are two regions which are a barrel and nozzle. In the barrel region, it is assumed that barrel is long and has large cross section area. The effect of viscosity is thus reduced. The dominant effect of viscoelastic material should be the effect of elasticity which is represented by a spring. However, in the region of nozzle, the area is considered small, thus the effect of loss modulus is dominant. The analogy is then modeled by a spring connected to a damper.

Such complexity of viscoelastic material causes a problem for controlling material extrusion by the displacement of piston. Regarding to Figure 27, the controllability of x_2 is depends on the correctness of viscoelastic modeling and knowledge of all parameters. However, the motion of x_2 eventually converge to x_1. For simplicity of the analysis the parameter is assumed constant. If K_v, M_v and C_v are spring, mass and damper of viscoelastic material,

$$M_v \ddot{x}_2 = K_v (x_1 - x_2) - C_v(\dot{x}_2) \qquad \textit{Eq. 42}$$

Then, if the system is linear-time-invariant, then the equation can be expressed in Laplace domain as

$$M_v\, s^2\, X_2 = K_v\,(X_1 - X_2) - C_v\, s\, X_2 \qquad \textit{Eq. 43}$$

The transfer function of input motion x_1 to output motion x_2 then is

$$\frac{X_2}{X_1} = \frac{K_v}{M_v\, s^2 + C_v\, s + K_v} \qquad \textit{Eq. 44}$$

Final value theorem

Final value theorem is a concept of control theory to determine the final value of a control signal at the steady state from a particular input. This concept can use to analyze the behavior at the steady state of a linear-time-invariant system.

In mathematical terms, the Final Value Theorem is applied within the Laplace domain. Consider a system characterized by a transfer function G(s) and an input x(t). The Laplace transform of the resulting output y(t) is represented as Y(s). The Final Value Theorem can be expressed as follows:

$$\lim_{t\to\infty} y(t) = \lim_{s\to 0} sY(s) \qquad \textit{Eq. 45}$$

To explain it differently, the ultimate value of the system's output as time extends towards infinity is equivalent to the limit of $sY(s)$ as s approaches zero. This theorem proves particularly valuable in examining a system's response to a step input, providing an approach for engineers and researchers to ascertain the steady-state value without explicitly computing the time-domain response.

It's important to note that the applicability of the Final Value Theorem hinges on the system's stability and the requirement that all poles of the transfer function possess negative real parts. Meeting these conditions ensures that the system attains a steady state, allowing for the valid application of the Final Value Theorem.

CHULALONGKORN UNIVERSITY

Analysis of steady state response from the model

The usage of final value theorem needs

- Linear-time-invariant system
- The system is stable.
- The solution of input and output exist.

From the assumption, the system has already passed the first condition for using final value theorem.

Next condition analysis is the stability of the system.

From Eq. 44, there are no zeros and poles from the system's transfer function. The denominator of transfer function is a quadratic function of s. Thus, Quadratic formula can be used for pole analysis.

The general formula of quadratic equation is

$$0 = a\,x^{\,2} + \,b\,x\, + \,c \qquad \textit{Eq. 46}$$

The solution of such equation can be expressed in closed form as

$$x = \frac{-b \pm \sqrt{b^2 - 4ac}}{2a} \qquad \textit{Eq. 47}$$

Substitute the parameters of the transfer function to quadratic equation, then the location of those two poles are

$$s = \frac{-C_v \pm \sqrt{C_v^2 - 4M_vK_v}}{2M_v} \qquad \textit{Eq. 48}$$

To prove the system stability, all poles need to be in left half plane which mean the solution of the pole in real part needs to be negative. If the positive pole exists, there is some condition that the system is unstable.

If the system unstable, the mathematic can be expressed by inequality, Re(s) > 0.

$$Re\left(\frac{-C_v \pm \sqrt{C_v^2 - 4M_vK_v}}{2M_v}\right) > \,0 \qquad \textit{Eq. 49}$$

The term M_v is represent the mass of the system. Since there is no negative mass and the square-root function only gives positive real number, the only case that needs to analyze is the plus condition. Then the denominator term can be left out as it is forever positive.

$$\sqrt{C_v^2 - 4M_vK_v} \,>\, C_v \qquad \textit{Eq. 50}$$

Since, in the reality, M_v, C_v, and K_v are indicated mass, damper, and spring, respectively, it needs to be positive. From such inequality equation, the highest number that can be produced by the right-hand-side is when the $4M_vK_v$ is equal to zero. In that condition, it is proved that inequality is invalid. Because square root of square of C_v is equal to absolute of C_v. Since, C_v is a positive number, the absolute of C_v then equal to C_v.

$$\sqrt{C_v^2} = \,|C_v| \,=\, C_v \qquad \textit{Eq. 51}$$

Thus, there is no solution of Re(s) > 0.

For Re(s) = 0, there are solutions that exist which is when M_v or K_v is equal to zero, or C_v is equal to zero. Thus, the pole is in the middle of the complex plane. However, mass, damper and spring always exist in the mechanical system. Such a case is impossible.

To conclude, the system from the proposed model is always stable since all poles are located in the left-half plane of the complex plane where Re(s) < 0.

The final value analysis is performed with two input types: step and ramp.

For step response, the response of x_2 is

$$X_2 = \frac{K_v}{M_v\, s^2 \,+\, C_v\, s \,+\, K_v}\,\frac{1}{s} \qquad \textit{Eq. 52}$$

The final value of x_2 can be written by

$$\lim_{t\to\infty} x_2(t) = \lim_{s\to 0} s\,\frac{K_v}{M_v\, s^2 \,+\, C_v\, s \,+\, K_v}\,\frac{1}{s} \,=\, 1 \qquad \textit{Eq. 53}$$

From the analysis, we can see that the steady state response of x_2 is equal to one which is exactly the same as the command input via x_1. Thus, for volumetric control which considered only amount of material and not considered its speed. The step input of motion of piston can perfectly control the motion of material in steady state.

For ramp response, the response of x_2 is considered by the velocity of x_2

$$s\,X_2 \,=\, \mathcal{L}\{\dot{x_2}(t)\} \qquad \textit{Eq. 54}$$

Then the response of velocity of x_2 is

$$s\,X_2 = \frac{s\,K_v}{M_v\, s^2 \,+\, C_v\, s \,+\, K_v}\,\frac{1}{s^2} \qquad \textit{Eq. 55}$$

The final value of x_2 can be written by

$$\lim_{t\to\infty} \dot{x}_2(t) = \lim_{s\to 0} s\,\frac{s\,K_v}{M_v\, s^2 \,+\, C_v\, s \,+\, K_v}\,\frac{1}{s^2} \,=\, 1 \qquad \textit{Eq. 56}$$

This result shows that the material feed eventually converges to the feed that is equal to the velocity of piston. Such result can prove that the proposed design can control the material feed rate over the LDM printing application. However, it does not guarantee the transient state when the velocity of piston changed. Fortunately, in the real application, material usually extruded with constant velocity.

CHULALONGKORN UNIVERSITY

Position controller

Extrusion experiments

5.1 Flushing experiments

This experiment was conducted to demonstrate the performance of the proposed design. The sample operation that was selected is flushing. Such operation is essential for 3D printing and extrusion process, serving several important purposes that contribute to the overall quality and reliability of the printed objects. One primary reason for flushing in 3D printing is to clear and clean the print nozzle or extrusion system. During the printing process, various materials, such as molten plastic or resin, are extruded through a nozzle to build up the desired object layer by layer. Over time, residues and contaminants can accumulate within the nozzle, potentially leading to nozzle clogs or inconsistent extrusion. Noted that, the material in 3D printing normally needs curing mechanisms for forming 3D structures via solidification. In LDM printing, such mechanisms usually involve air or temperature. The material in the tip of nozzle is usually affected and changes their properties. Flushing helps prevent these issues by purging any residual material from the system, ensuring a clean and unobstructed flow of material during subsequent printing sessions. This maintenance step is particularly crucial when switching between different materials or colors, as it helps prevent cross-contamination and maintains the integrity of the printed object. Additionally, flushing can also eliminate air bubbles in the material, contributing to smoother and more precise printing.

Herein, the flushing process of chocolate fudge was performed six times. In the first half of the experiment, different controlled feed rates of 1, 2, and 3 mm/s were executed. Then, in the second half, the controlled pressures at motor voltages: 8, 10, and 12V were implemented. The pressure controller in this experiment is built upon simple voltage control. This controller gives stable current when the system is at constant velocity. To compare both extrusion method, the amount of material extruded for each attempt are equalized, extrusion was halted when the piston position, 3 mm from the starting point, was reached. The piston's speed and the motor's electrical current were measured over time.

จุฬาลงกรณ์มหาวิทยาลัย
CHULALONGKORN UNIVERSITY

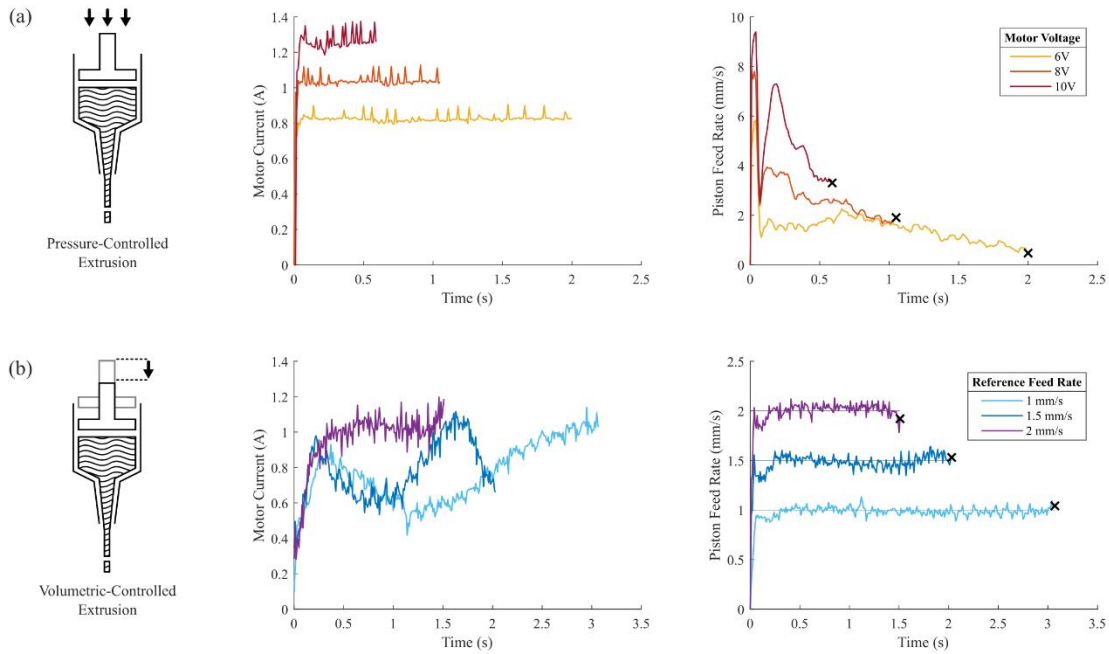

Figure 28 Experimental data obtained from the flushing operation of the different modes. Pressure-controlled extrusion (a) is actuated by 8, 10, and 12 V. Volumetric-controlled extrusion (b) is commanded at the piston's reference feed rate of 1, 2, and 3 mm/s. Extrusion ends when a piston displacement of 3 mm is reached, as signified by black "X".

In Figure 28, both the measured current and piston feed rate, from the pressure-controlled and volumetric-controlled flushing of chocolate fudge, are shown. Piston feed rate was calculated via the differentiation of the measured piston position over time. The differentiation was computed by Backward-Euler method. The motor current represents the torque generated from the motor, corresponding with the pressure at steady state. The data was collected at 100 Hz by microcontroller (STM32 mcu) inside the proposed machine. Then such data was transmitted to a computer via serial communication.

In the pressure-controlled flushing process, the constant voltage applied to the motor and the piston initialized the flow of the print material from its resting state. This event resulted in the surge of the motor's electrical current to certain values. The current is seen to stabilize around the values up to the end of the process. From the observation, the fluctuation of piston's speed does not disturb the current. Noted that, the motor generated back-EMF when the motor's coil spins and then cuts through magnetic field. The higher the angular speed, the more back-EMF is produced. The fact that current tends to stable after around 0.1 s while the piston feed rate is yet in transient shows the dominant of resistance load over back-EMF effect. Furthermore, the current signal also represents the pressure inside the material. The generated torque from motor current pushes the piston forward to compress the material. However, in the period that system gains acceleration, the current does not perfectly reflect the pressure because some of the torque is split to build up momentum. But, in this case, chocolate fudge is relatively viscous, thus, the acceleration is considerably small.

In Figure 52 (a), a rise time of current signal is about 0.1 s however the piston speed is varied depending on applied voltage. All three experiments show peak velocity at first then abruptly slow down. Such effect is caused by the elasticity of viscoelastic material. The elasticity allows the material to be compressed. From this evidence, it may display the complex modulus of chocolate fudge: the low amount of loss modulus compared to storage modulus. Due to the lack of loss modulus, the material allows fast response which is represented by such peaks. From flushing at the voltage reference of 10 V, there are two peaks of piston's speed. This behavior does not follow the simple rheology model that material can be compressed, and the flow is highly viscous. The signal shows two times of compression. This evidence confirms the complexity of rheologic mechanism of viscoelastic material extrusion. Those two compressions may have occurred from accidental clogging, or the flow mechanism of chocolate fudge suddenly changed. In contrast, in the case of 6 V, the motor's speed shows more stability and aligns with the model. Lower voltage may produce less stress to the material and allows material to response in more linear. From the graph, the rise time to steady state of motor's speed (6V) is equal to 0.1 s.

In the volumetric-controlled flushing process, the motor current displayed a relatively slower rise. The complex behavior of material storage and loss modulus triggered a large magnitude of fluctuation in the electrical current with diverse behavior, depending on the applied feed rate. The pressure from each feed rate did not appear to converge to any certain value in the 3 mm extrusion time frame. As far as the information is given, it is difficult to prove the steady state convergence. Although, the lack of knowledge in steady state, from this result, it may be concluded that the pressure cannot be guarantee via the volumetric-controlled.

From both experiments, it is evident that pressure control flushing process provides better performance, giving faster rise time and guarantee pressure inside the syringe. It is seen that current rises faster in pressure control (rise time 0.1 s) than volumetric control (reach peak of first slope at around 0.3 s). Moreover, the pressure control approach with 6V voltage reference may give a promising solution for the flushing process. Regarding the purpose of flushing, the extrusion application should always start at the same state. Regulating initial pressure can give better repeatability. Moreover, the volumetric control shows poor precision over current signal where the pressure is implied.

To conclude, pressure control demonstrates more promising results over the volumetric control because faster rise time and more stability. Such stability is useful to give precise initial state to extrusion applications. Thus, the repeatability of applications is enhanced.

5.2 Line extrusion experiments

3D printing is one process that can form 3D structure is to lay a layer on top the previous layer. This process is done repeatedly with precise deposit location and accurate amount. The outcome can be formed precisely. This technique can be applied to material that is in fluid state then solidified. Of paramount importance in the 3D printing process is the nuanced control of line width, dictating material extruded from the nozzle during each pass. This precision is essential to resolution and ensuring the cohesive adhesion of successive layers.

From such necessity, the regulation of extrusion flow is in need. However, the complication from the rheologic mechanism of molten material is very difficult. By the process of extrusion, the material needs to be fluid enough to flow through nozzle and form infinite type

of shape. But, after the extrusion material needs to be solid enough to hold itself over the gravity field. Such phase change is difficult to control to happen in the right position and right time. This effect also influences the rheology. The behavior of material flows can be varied over time. Thus, the regulation approach for the extrusion flow is demanded.

In this research, the hypothesis is that the volumetric flow control can give better precision of linewidth. This can be done by the position control mode over the proposed design. Furthermore, the pressure control mode is also available in the same design. Thus, the experiment was done to extrude 3 materials: biogel, chocolate fudge, and silicone sealant. The linewidth of each material and each approach was then compared. The linewidth of each material was measured by a camera with telecentric-lens. The image of the result is fully orthographic and then physical size was calibrated. The results were then applied with image processing to get the edge of line width.

Experimental setup

To print a line of material, the proposed extruder is designed to install at a cartesian robot. Such robot comprises of 3 linear axis of Snapmaker linear module. Then all axis was controlled by Mega2560 mcu that has been installed a 3D printing Firmware: Repetier. The proposed extruder has a mechanical interface that contains a permanent magnet, pogo pins, and locating bushes. On the 3D printer side, the interface also has an iron bar, pogo pins, and locating pins. Both interfaces can be easily assembled and disassembled via human hand. The mechanical interface allows 6 electrical pins to be connected via pogo pins.

Six wires contain supply voltage, ground, UART_TX, UART_RX, step, and direction. The first two wires have a duty for supplying power for all modules in an extruder side. The current can be as high as 3 A to drive a dc motor. After that, UART_TX and UART_RX are signals for Universal Asynchronous Receiver and Transmitter (UART) communication protocols. Such protocols are a serial communication protocols for transmitting the data between a proposed extruder to a computer. Furthermore, some of parameters such as PID and feedforward gain can be adjusted via these lines. By adjusting the gain, the operation mode of extruder can be changed on the fly. The last two signals: step and direction are common signals to drive stepper motor in the domain of 3D printer. Such signals are considered high speed and real-time signal because the stepper motor needs to move in fast motion while maintaining synchronization to the others. To achieve forming 3D structures, the material needs to be deposited in the right places, x, y, and z axis of robot need to precisely synchronize with extrusion axis. In summary, six wires interfaces can supply the energy source and support large data communication via UART and real-time motion synchronization via step-direction.

The sample material is chocolate fudge, biogel, and silicone sealant (around 50,000 centipoise). Those three materials perfectly reflect the application of LDM 3D printing that can be used in various industries, e.g., food printing with chocolate, cell printing with biogel and engineering and construction with silicone sealant. The material was loaded in syringe before the experiment. The loading process needs to be careful about the bubble inside the material. The bubble can cause disturbance in flow and non-uniform linewidth because amount of deposit material is reduced by portion of air bubble.

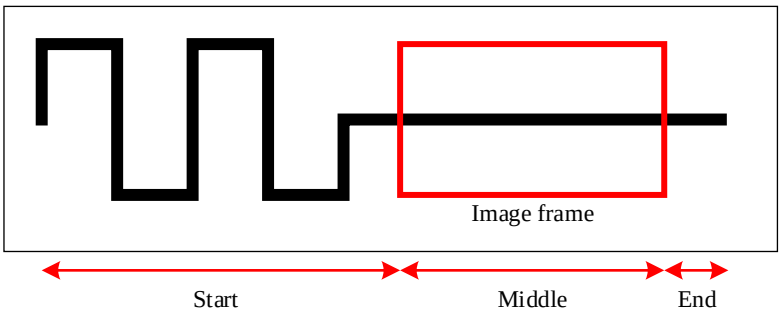

Figure 29 the pattern that designed for line-width measurement. The pattern contains start, middle and end period. The start period allows material extrusion to be in transient response and does not disturb the measurement. In the middle period, the material is assumed to be steady, and the measurement was taken. The end period is the places where the extruder stops and then park, some material can be oozing.

In Figure 29, the pattern is designed for image-based linewidth measurement. The image was taken in the red rectangular frame. This pattern contains start, middle and end zone to associate with the starting period of extrusion, stable flow, and then stop. In the starting period, the extrusion flow can be affected by the elasticity of the viscoelastic material. Such materials allow to be compressed. Consequently, the material in the nozzle does not experience extruding. Furthermore, to develop steady flow, some material needs to be flushed. The zig-zag line in the starting zone is designed for ensuring the steady flow in measurement period (middle). Such line has a long length that material can be extruded and developing well flow. After entering the middle zone, material is assumed to flow at a constant rate. The line width is measured at this point. The image was taken and cropped in this rectangular frame. Finally, the ending period where nozzle is stopped to move and extrude. This area can suffer from oozing. Such behavior is caused by residue stress that is left inside a syringe. The stress still generates enough pressure to force material flow. In this area, the material can be over extruded and should be excluded from the observation of the experiment.

จุฬาลงกรณ์มหาวิทยาลัย
CHULALONGKORN UNIVERSITY

Figure 30 the measurement tool for capturing the printed result using telecentric lens with a Basler camera.

After finishing extrusion process, the sample in experiment was brought to capture via telecentric lens camera. The camera is a BASLER acA3088 camera which is embedded with Sony IMX178 CMOS sensor. It can deliver up to 59 frames-per-second at 6.4 MP resolution. The image was received by Pylon software which offers reliable, certificated driver for Basler camera. It is a powerful and simple interface for many vision sensors. The software offers an easy approach for configuring, e.g., gain and exposure time, via graphical interface. A telecentric lens that is connected to the camera is designed to have constant magnification which eliminates the perspective error. It is because the lens allows only parallel light to enter the camera. Furthermore, the parallel rays also minimize shadowing effect, enhancing the quality of capture image. With these features, such lens is widely employed in metrology, inspection, and manufacturing for application where the measurement and accuracy are paramount. The ring light LED is also installed to the image station for supply light source. The radial symmetry of the source reduces the shadow on the object, reduces the challenge in image processing.

After an image has been captured, the observed image was then transformed to grayscale for image processing. Next the image was applied to convolution of Sobel operator. Such an operator enhanced the contrast of image by accentuating the color difference. This mechanism is based on the assumption of edge occurs where the color is changed. Furthermore, Sobel operator can have two type that can detect the edge in horizontal or vertical axis. The Sobel convolution of horizontal axis can be written mathematically by

$$\boldsymbol{G_x} = \begin{bmatrix} 1 & 2 & 1 \\ 0 & 0 & 0 \\ -1 & -2 & -1 \end{bmatrix} * \boldsymbol{A} \qquad \textit{Eq. 57}$$

where $\mathbf{A}$ is an input image and $\boldsymbol{G_x}$ is an edge-enhanced image.

The enhance-edge image is then applied to absolute in each pixel and then do thresholding to select the edge of material line print. The threshold value is acquired by fine-tuning process.

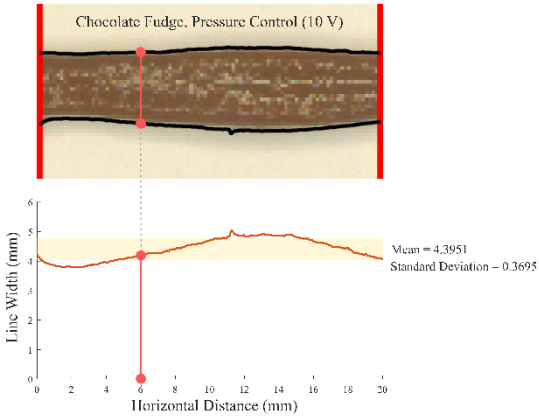

Figure 31 Line width extraction process. The images of the lines are processed using a binary thresholding technique to find the upper and lower bounds of the lines. Then, the number of pixels between the upper and lower bound at the same vertical position are counted. These numbers are obtained along the selected portion of the printed lines. Subsequently, the mean and standard deviation of these numbers are calculated.

After the edge pixel is determined, the result image is a binarize matrix. Each image was gradually scanned by vertical axis through the image horizontal axis. After hitting to edge pixels, the distance between those two pixels is calculated and then the unit is adjusted from pixel to millimeters.

The information of linewidth is a series of widths on the horizontal axis. The variation of width can be seen in Figure 31 (lower). To evaluate the quality of linewidth, standard deviation is used. If X_i is a linewidth at any vertical column of the image, $\bar{X}$ is an average of linewidth, N is a number of all vertical column, then standard deviation, σ, is

$$\sigma = \sqrt{\frac{\sum_{i=1}^{N}(X_i - \bar{X})^2}{N}} \qquad \textit{Eq. 58}$$

The quality of linewidth can be considered by standard deviation. The linewidth should have enough precision which means the width should remain constant. As the line continues straight, the standard deviation results low. If the width fluctuates, the standard deviation increases. Besides, the average value will be presented in the report. Such values can be represented the goodness of linewidth control. But the error of average width can be compensated by earlier parameter tuning if the precision of linewidth is high enough.

Experimental results

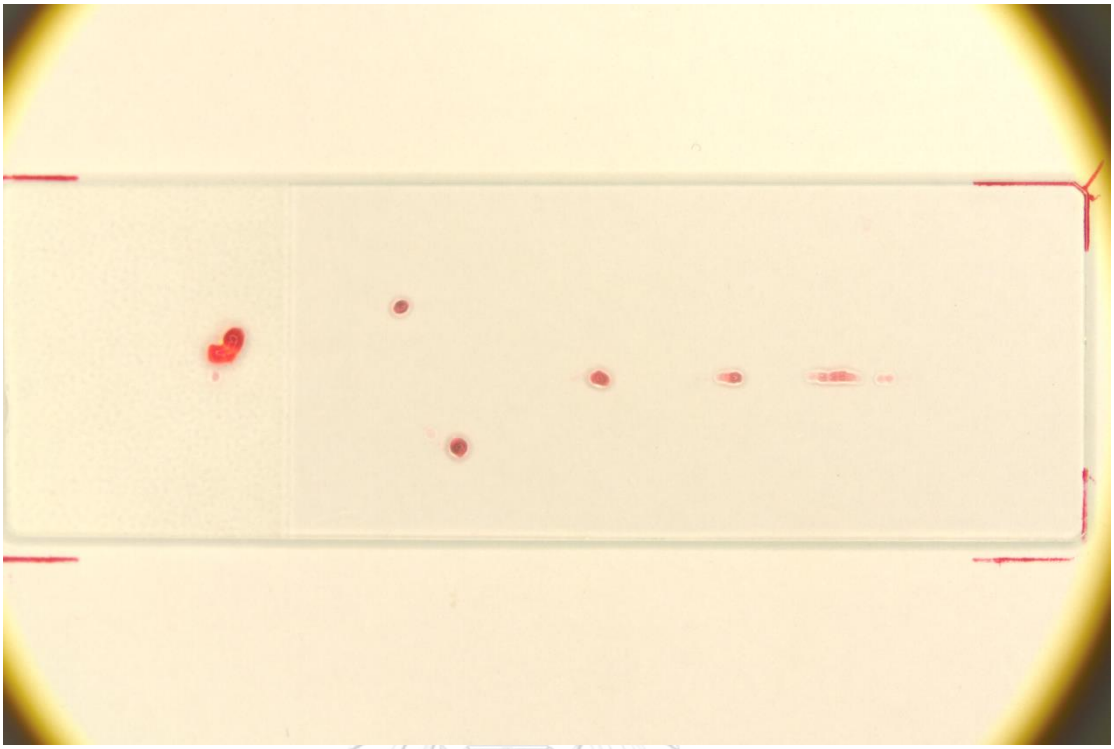

Figure 32 the result of biogel printing using pressure control mode at 4V (constant voltage input)

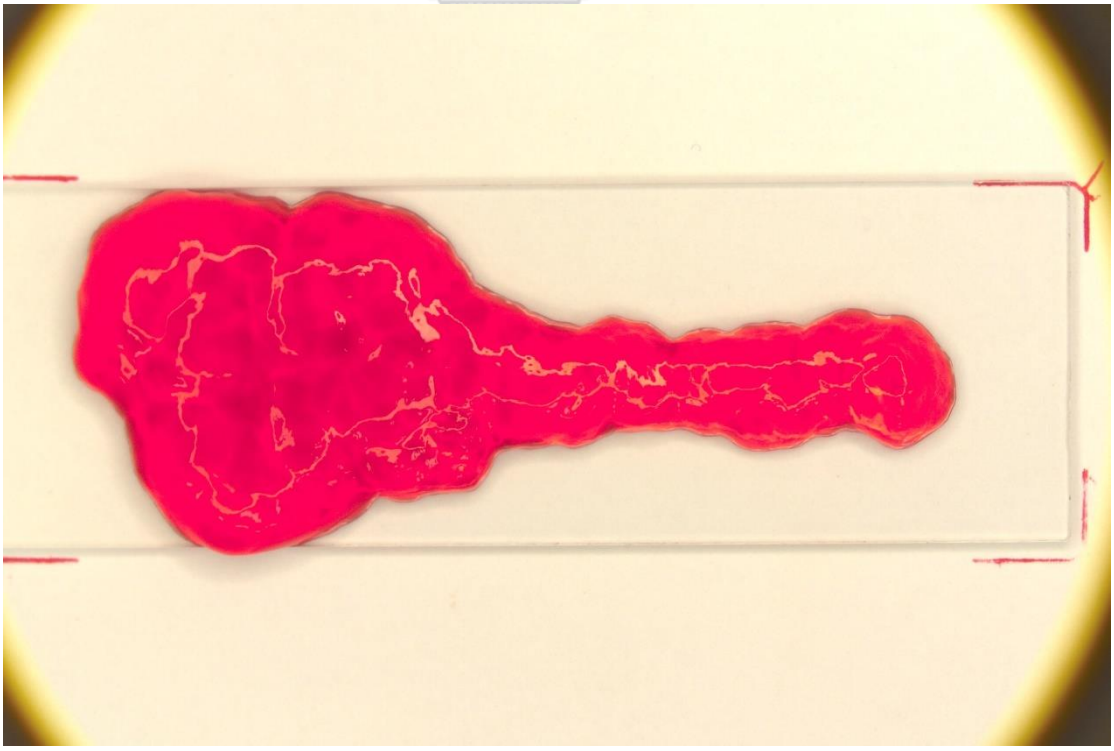

Figure 33 the result of biogel printing using pressure control mode at 6V (constant voltage input)

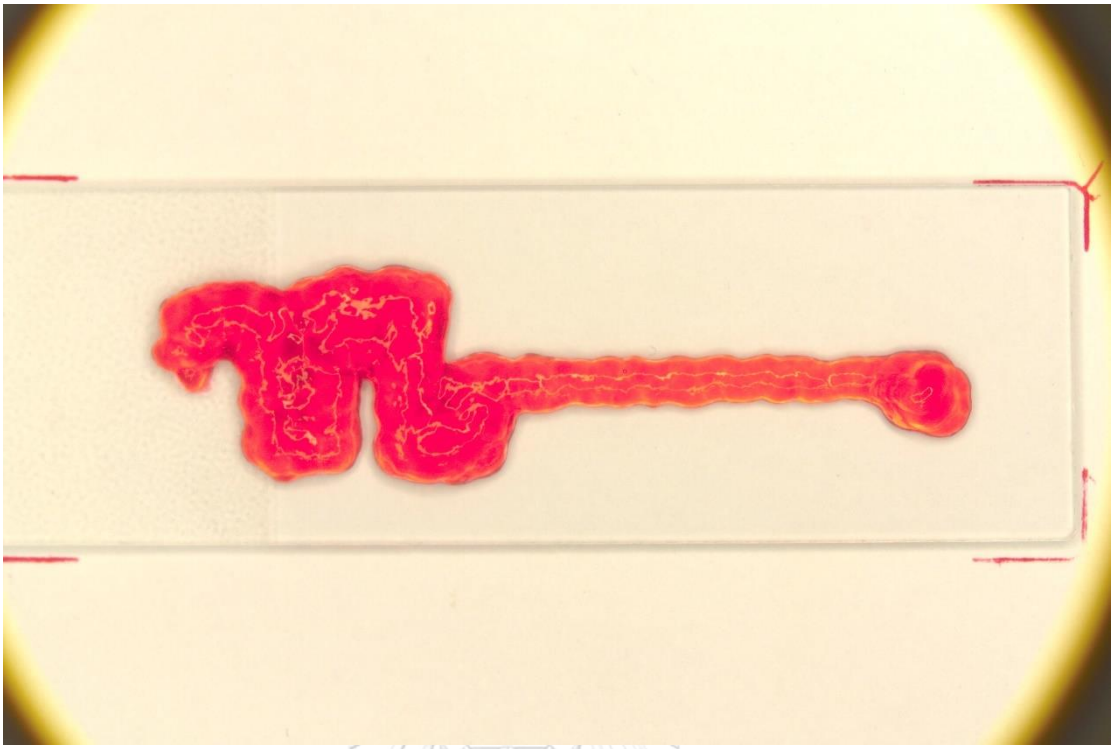

Figure 34 the result of biogel printing using pressure control mode at 8V (constant voltage input)

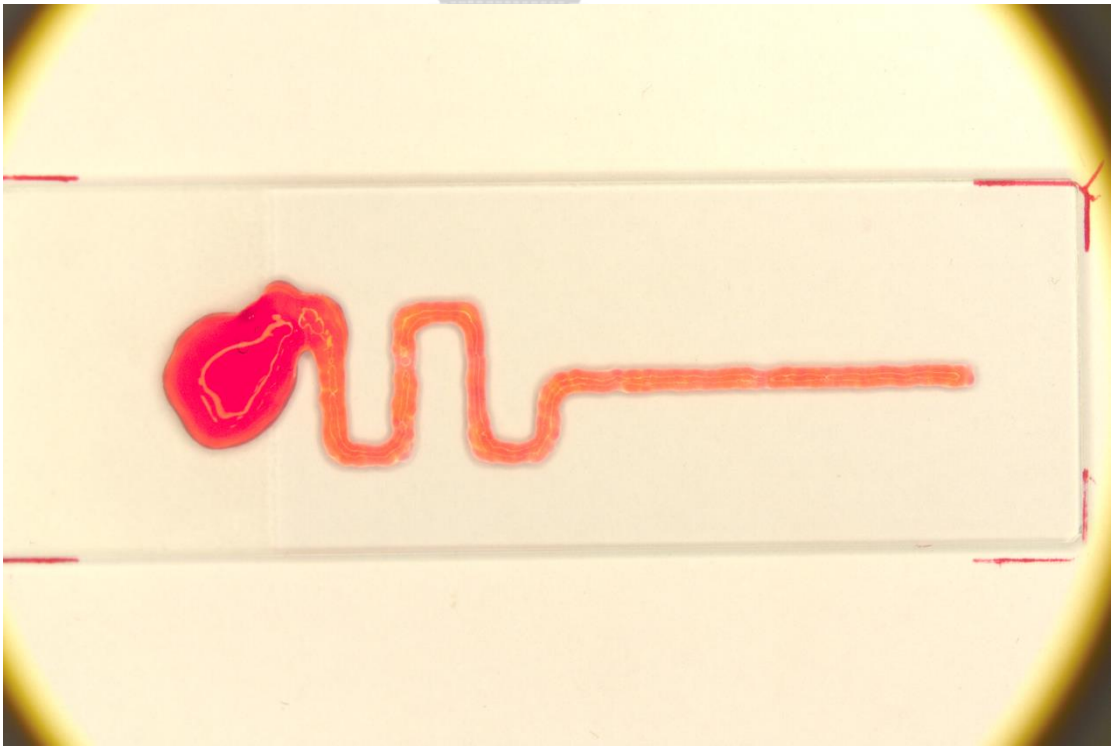

Figure 35 the result of biogel printing using volumetric control mode at 4.17 mm^3/s

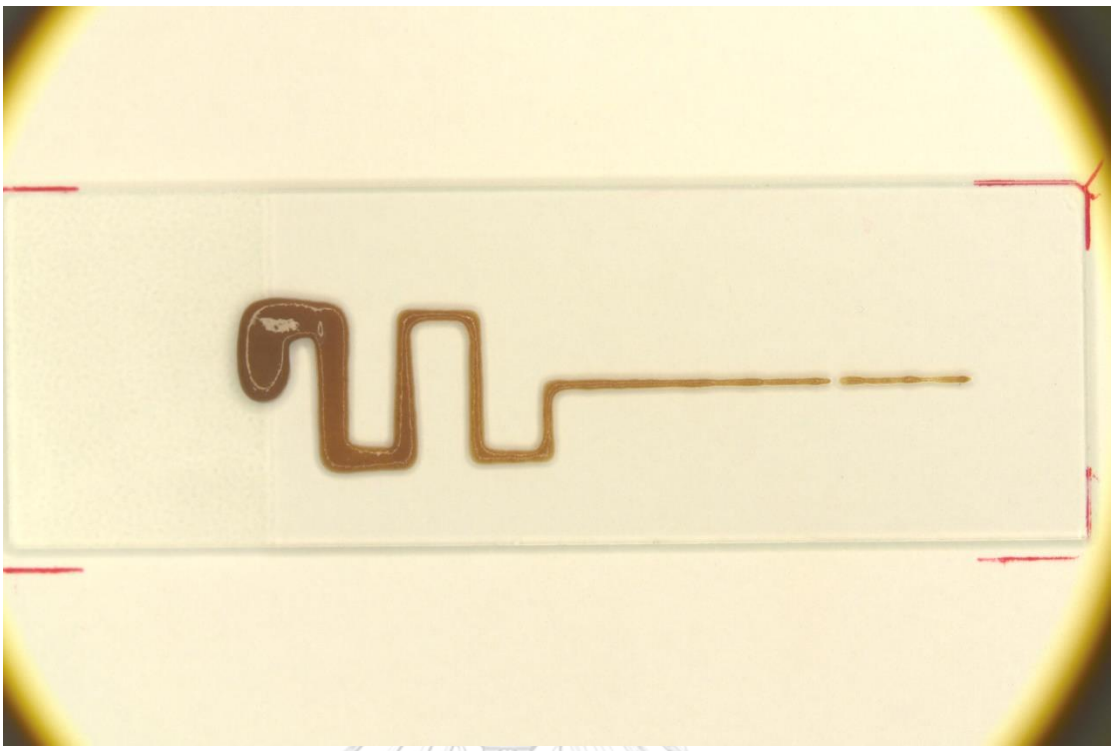

Figure 36 the result of chocolate fudge printing using pressure control mode at 6V (constant voltage input)

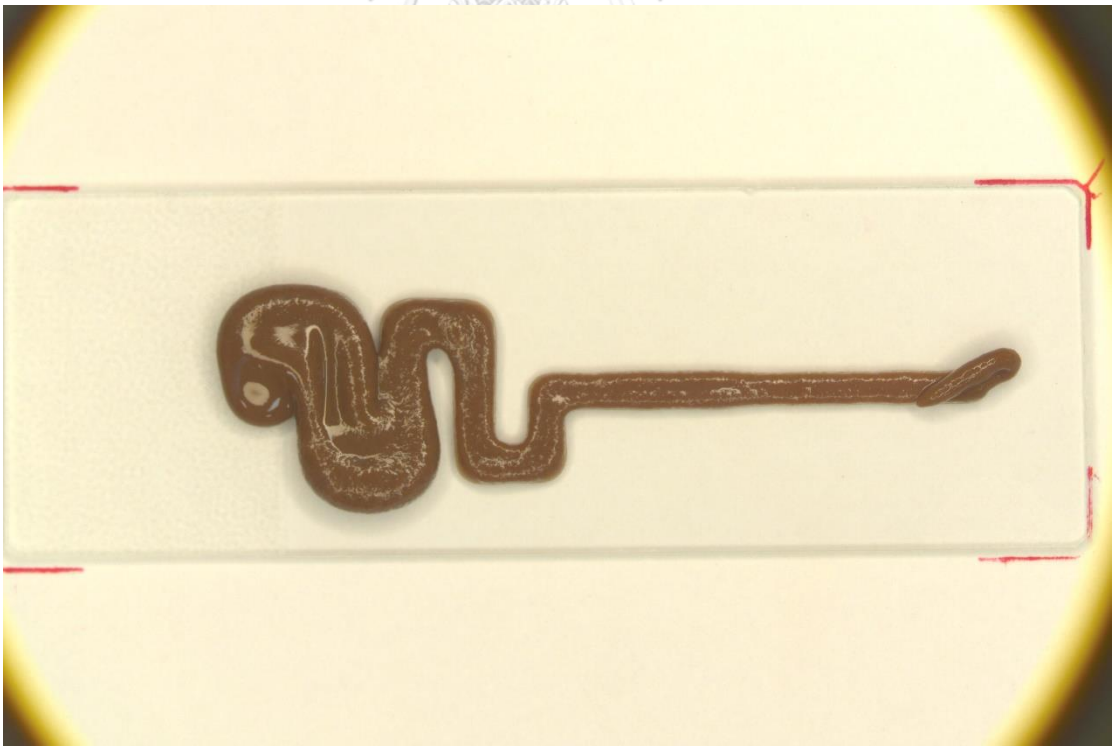

Figure 37 the result of chocolate fudge printing using pressure control mode at 8V (constant voltage input)

Figure 38 the result of chocolate fudge printing using pressure control mode at 10V (constant voltage input)

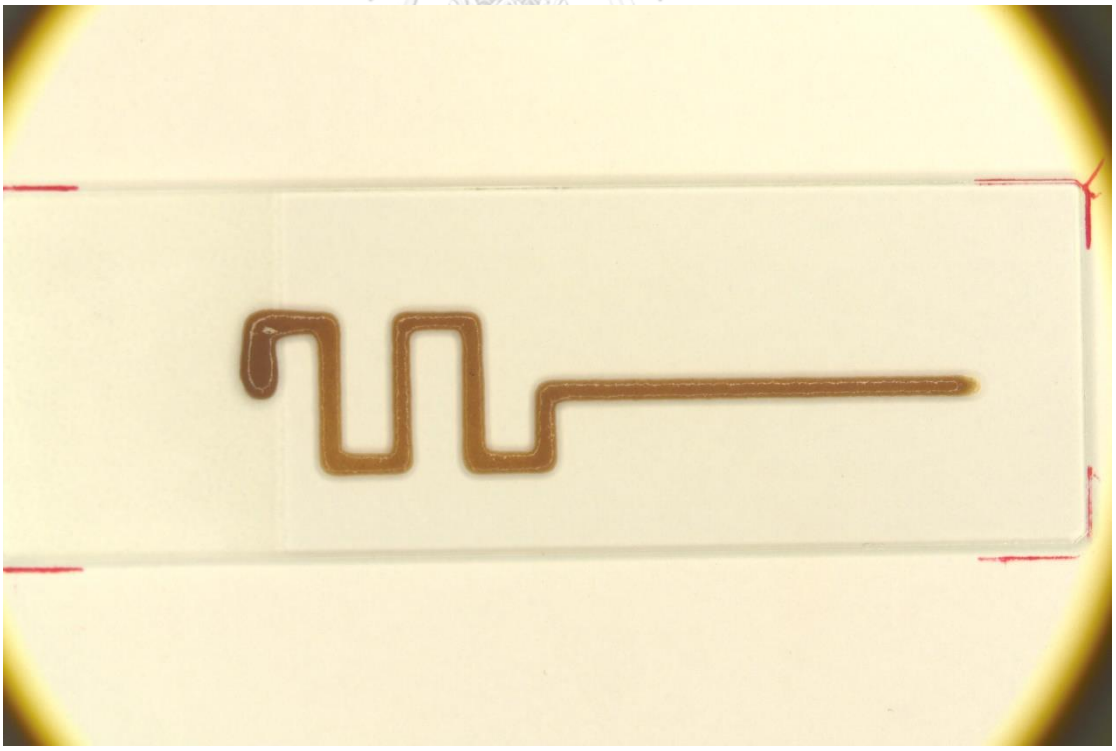

Figure 39 the result of chocolate fudge printing using volumetric control mode at 4.17 mm^3/s

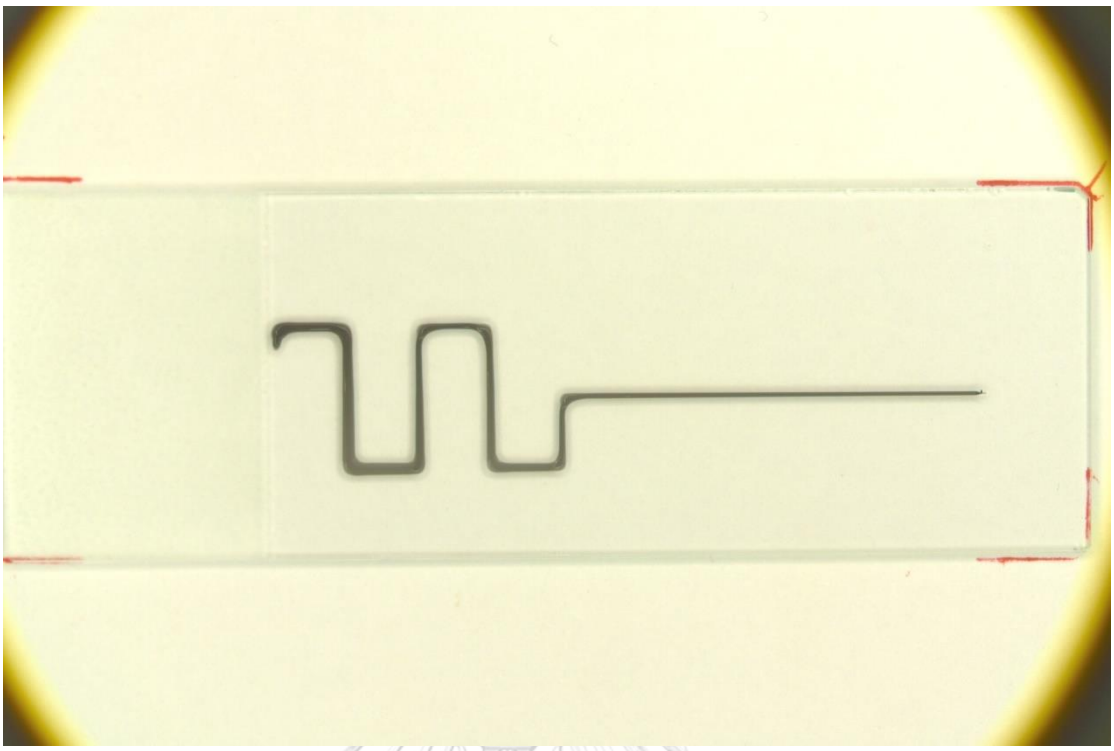

Figure 40 the result of silicone sealant printing using pressure control mode at 6V (constant voltage input)

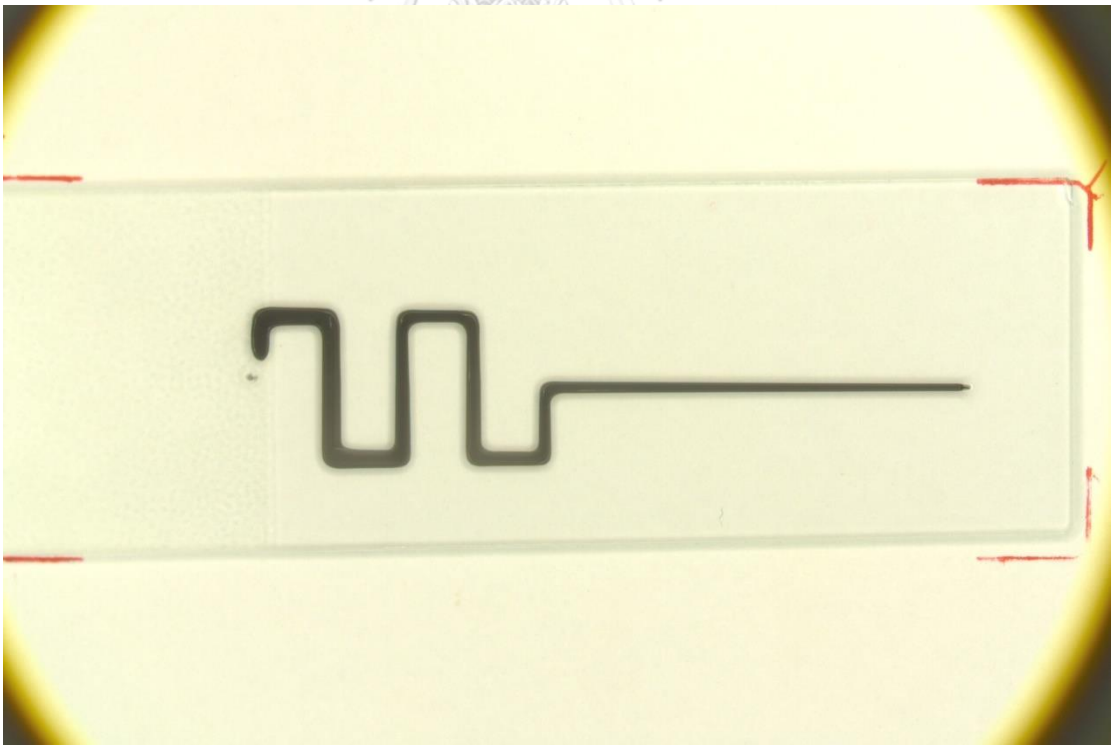

Figure 41 the result of silicone sealant printing using pressure control mode at 8V (constant voltage input)

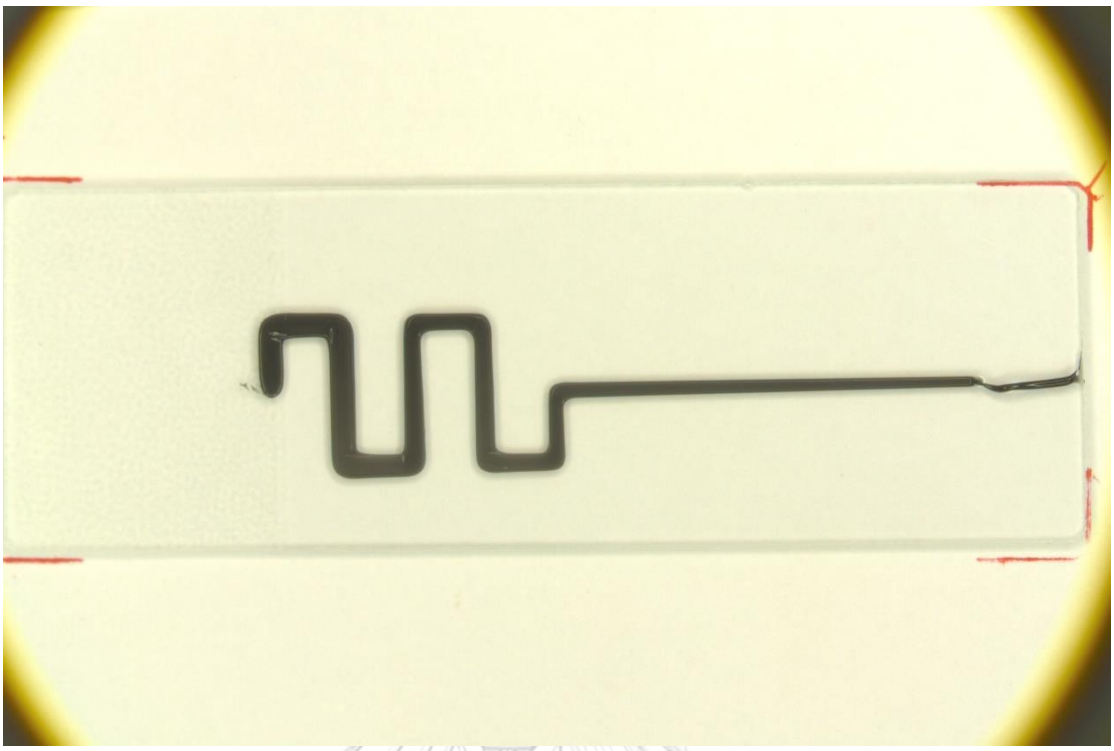

Figure 42 the result of silicone sealant printing using pressure control mode at 10V (constant voltage input)

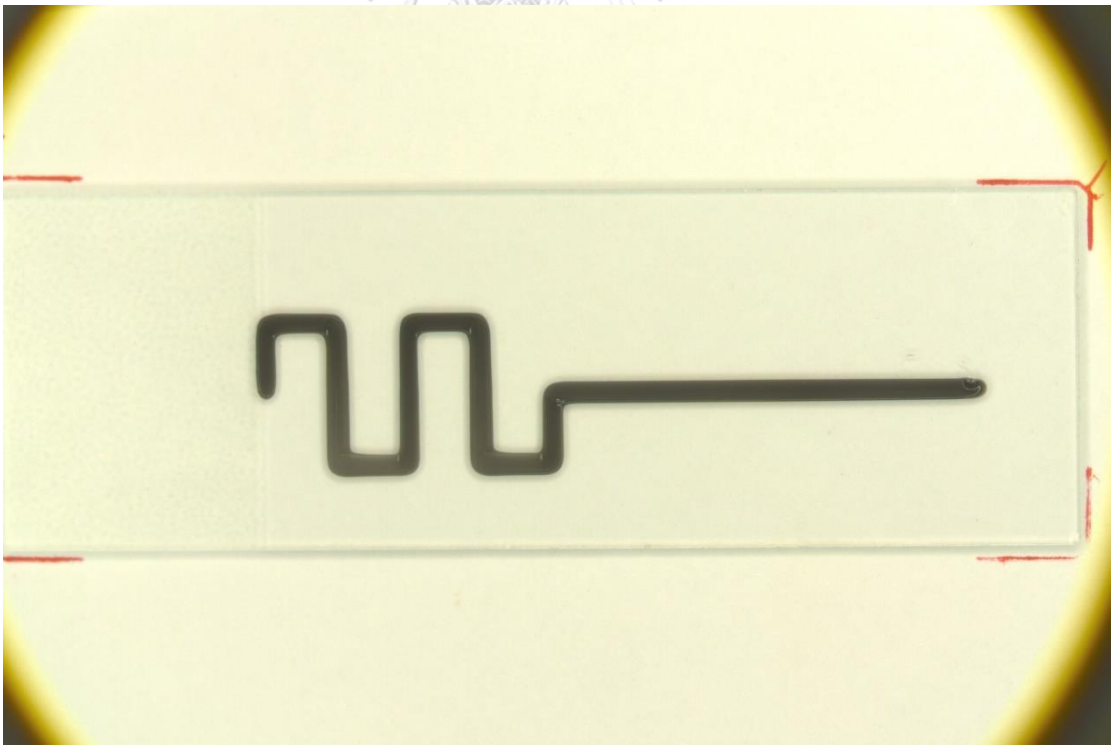

Figure 43 the result of silicone sealant printing using volumetric control mode at 4.17 mm^3/s.

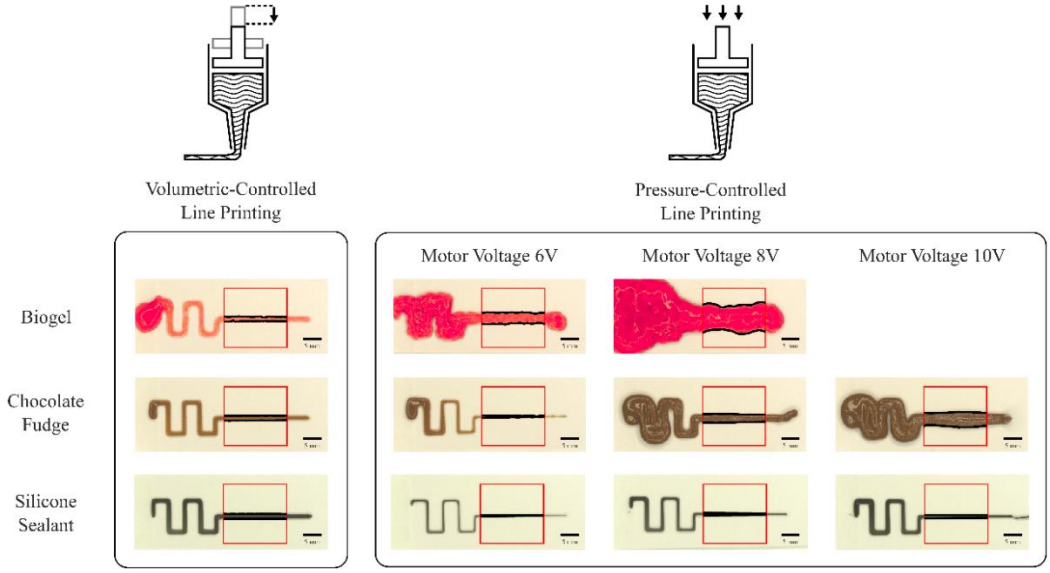

Figure 44 The printed lines using volumetric-controlled and pressure-controlled extrusion. The selected region is indicated by red squares. These are area which mean and standard deviation of line width are extracted. The black scale bar in the pictures is 5mm in length.

From Figure 44, the result shows processed images of linewidth for each material: biogel, chocolate fudge, and silicone sealant. The group on the right show linewidth from volumetric flow mode extrusion, and the left shows linewidth from pressure control mode at the voltage of 6, 8, and 10 V. The red rectangular frame is indicated the area of line that used for analyzing linewidth. The black edge illustrates the output edge from Sobel operator and binary threshold.

From the observation, the linewidth from pressure control extrusion illustrates the high variation depending on both the given voltage and material. Considering variation of voltage, higher voltage results in more material extruded which can be seen as wider linewidth. From this experiment, it can be seen that there is the optimum voltage for each material. For example, biogel is suitable for extruding at 6 V. At voltage of 8 V, the width of biogel shows fluctuation. From Figure 32, the extrusion by 4 V gives poor result by the material is under extruded. The line of biogel is not fully formed. With chocolate fudge, the optimal point is 8 V. However, the pressure extrusion of silicone sealant gives well quality in both 6, 8, and 10 V. Noted that, the optimum voltage should be varied by the extrusion machine and nozzle size which impacts on the viscous friction of material. From these results, the extrusion by pressure control gives more extrusion when the applied voltage is higher. The variation of material can cause dramatic changes in quality of linewidth.

In case of volumetric control, the printed line tends to remain straightness. The lines from different materials are likely to be similar. The line from biogel printing shows unevenness however for chocolate fudge and silicone sealant is seen smooth. Compared to pressure control across the materials, biogel gives the worst result for smoothness of the line. This effect still appears in volumetric control, but such effect is reduced. The increase in smoothness of biogel shows effectiveness of volumetric flow control over pressure control.

This benefit can suppress the effect of poor flowability and extrudability of material. Furthermore, volumetric flow control can suppress the effect of viscous friction from viscosity in material. The viscous friction causes linewidth variation over the material. The result evident that the line in volumetric control tends to similar which independent on materials.

Table 4 Mean Line Width(μ) in the unit of mm with Standard Deviations(σ). The lowest standard deviation value for each material is indicated by [1]

	Position Controlled		Pressure Controlled					
			Motor Voltage 6V		Motor Voltage 8V		Motor Voltage 10V	
Materials	μ	σ	μ	σ	μ	σ	μ	σ
Biogel	1.4254	0.1080[1]	3.4999	0.1890	8.4479	0.6639	N/A	N/A
Chocolate Fudge	1.5267	0.0394[1]	0.4972	0.1683	2.5965	0.1945	4.3951	0.3695
Silicone Sealant	1.5531	0.0142[1]	0.2866	0.0347	0.6574	0.0665	0.9613	0.0725

In Table 4, the numerical analysis of linewidth is shown. The quality of linewidth is described by mean (μ) and standard deviation (σ). Low standard deviation refers to smooth line and high standard deviation indicates fluctuated line. The smoothest line from all experiments is silicone sealant that printed by volumetric control where standard deviation equal to 0.0142 mm. For each material, volumetric control gives the smoothest line. For biogel and chocolate fudge, standard deviations are 0.1080 and 0.0394 mm, respectively. Such evidence reconfirms the effectiveness of volumetric control to regulate the printed linewidth. Pressure controlled line results in high standard deviation. The poor printability of each material can be observed by this table. Silicone sealant is the greatest property among sample materials. Even in pressure controlled, standard deviations are still reported in relatively low amounts. Furthermore, the volumetric flow control also gives controllability over viscosity change. The variation of material tends to not affect the average width of printed line. Compared to pressure control mode, the average width is highly different. The average linewidth of chocolate fudge and silicone sealant are very close at 1.5267 and 1.5531 mm, respectively, which deviate only 0.0264 mm. Thus, the volumetric control can be used across any material where the linewidth is still in control. There is no need for prior calibration.

CHULALONGKORN UNIVERSITY

In conclusion, the material extrusion needs to use volumetric control to regulate the smoothness of linewidth. The volumetric control can suppress the poor extrudability of material and can be used across any material with no need for prior adjustment. The extrudability of material still affects linewidth quality however the quality of linewidth by volumetric control is significantly enhanced.

5.1 Clog detection experiment

Apart from utilizing flexible actuation, the sensed pressure and volumetric flow rate can be used to perceive the properties of the print materials. The ability to perceive real-time properties of the print material was validated through a heterogenous mixture extrusion test. As shown in Figure 45, the syringe containing the mixture was prepared. The volumetric-controlled extrusion was executed on this non-homogenous mixture at the reference piston feed rate of 1 mm/s. The piston feed rate was logged over time together with the motor's electrical current which can be used to validate motor torque.

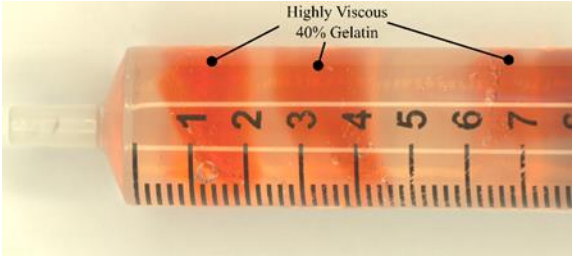

Figure 45 The heterogenous mixture of 40% food-grade gelatin in water solution (red) deposited in its 5% counterpart (clear). The mixture is stored in the syringe.

The heterogenous material was prepared by the mix of low concentrations gelatin (5%) and high concentrations gelatin (40%). The high concentrations are imbued with red color. At first, the high concentrations gelatin was produced by 40% gram-per-volume gelatin powder and 50°C water. The solution was left to cool. After that, gelatin was solidified. The solid gelatin was split into smaller forms ready to put inside a syringe. Next the low concentration gelatin was prepared with 5% gram-per-volume gelatin powder and 50°C water. The low concentrated solution was poured into the syringe which a syringe's piston was removed and the syringe nozzle was completely sealed. Then the high concentrated gelatin was picked up and added to the low concentrated solution. The syringe was then left to cool down. After all the material inside syringe was at room temperature, the experiment was ready.

The material was fed with constant speed at 4.17 mm^3/s via volumetric control. All control signals were logged and transmitted to a computer at a rate of 100 Hz. A camera (Logitech C920) was installed to capture the material and syringe. The capture video was then processed by image processing to synchronize the motion and enhance the high concentration of gelatin. The synchronization process was done by capturing the piston motion. After that, the video was processed with color thresholding to highlight the concentrated material that clogs inside the nozzle.

Time synchronization

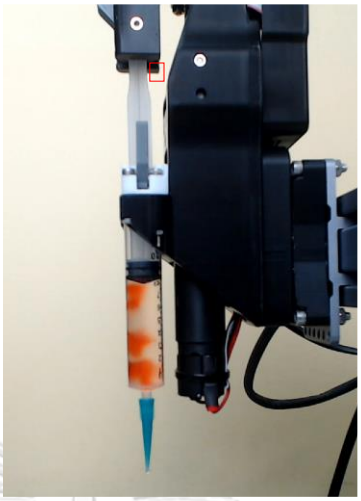

Figure 46 the sample image in captured video. The red rectangular frame indicates the region of image that was used for time synchronization.

It is impossible to start the camera capture and command the proposed design at the same time. Because the communications integration between a computer and proposed machine and between a computer and camera.

For communication to the proposed machine, such machine was designed to cope with real-time motion synchronization via step-direction wires. However, those wires are connected to the mainboard of the 3D printer. The 3D printer communicates to a computer via USB-serial communication. Thus, when the extrusion was commanded. The command is then stored into some buffer and copy its memory and then transmit it via usb. After that, the message was then converted to UART with a USB-UART chip. Later, the message was received by 3D printer mainboard. The mainboard then stored it into some buffer and then did execution. For a camera, the computer needs to communicate with an embedded microcontroller inside camera to configure it and request video streaming via USB. Thus, the delay of a camera capture is unknown. Noted that, a video capturing process is not designed to start in a deterministic time. Through all these layers of communication, it is difficult to determine the time delay. Furthermore, the time that message was stored in some buffer is also non-deterministic. Thus, control signal and video capture need to be processed with time synchronization before an analysis.

Figure 46 shows an example frame of captured result. The red rectangle indicates the region that is used for synchronizing time. That region contains a rigid body of a piston and highly contrasts with the background. Such rigid body is linked to motion of a ball screw which also linked to the motor shaft. Thus, the motion of that rigid body can be used as indicator of starting point of the process.

The image was cropped into the red rectangle. Next, the grayscale was applied to the image. Then compared motion by calculating the differentiation of pixel to the resting point. If p_i is a value of each pixel in image and $i = 0$ is a starting frame, each pixel value of the deviation image from starting point can be expressed as

$$\delta p_i = |p_i - p_0| \qquad \textit{Eq. 59}$$

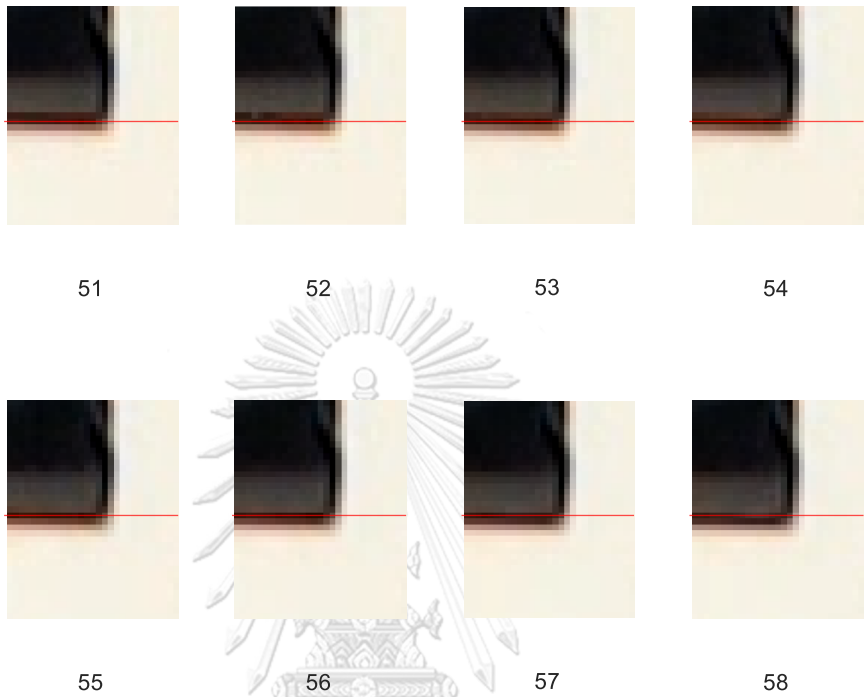

Figure 47 the region of interest for synchronization of time in various frame.

Figure 47 shows the group of images that has been cropped between frame 51 to 58. The red line is a guideline for motion starting. From frame 51, the black region is on the top of red line however, in frame 58, it can be seen that the black region is gradually creeping to the lower of the line. This comparison is difficult for human judgement for humans. The pixel subtraction method that presented in Eq. 59 was implemented on those images to analyze the starting point of motion.

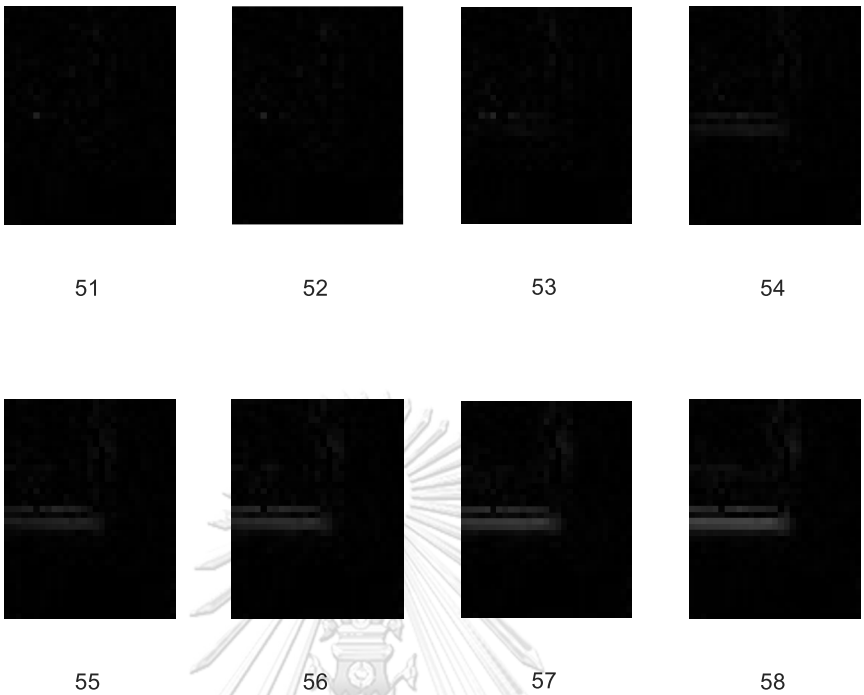

Figure 48 image of the deviation from resting postion in various frame.

Figure 48 illustrates the pixel difference between starting point frame and the frame 51-58. In the frame 51, the image is completely dark, implied that the frame has no difference to the starting frame. However, in the frame 58, white tainted shows the movement of a piston that moves downward. The white pixel shows the change on image pixel.

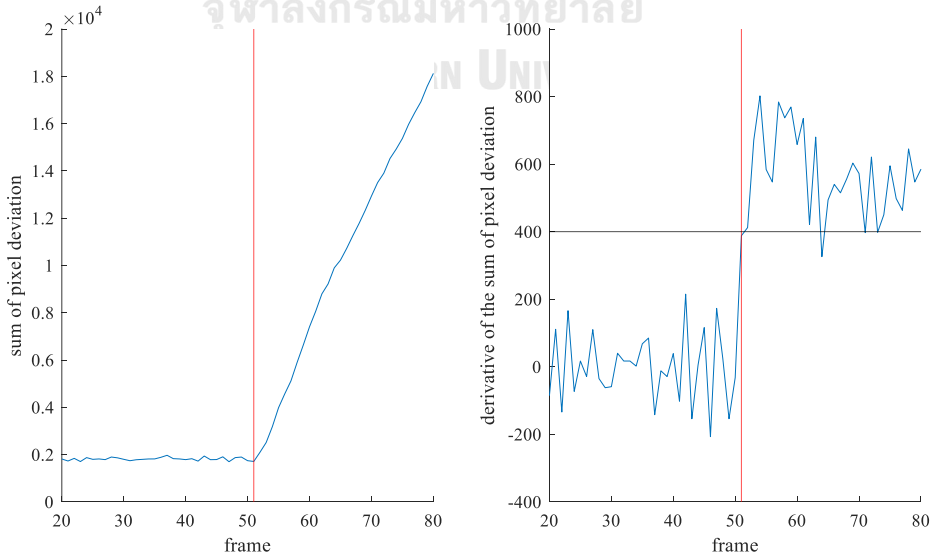

Figure 49 The left graph shows sum of absolute deviation of frame from starting point. The right graph shows the derivative of the sum.

Figure 49 shows the insight information of the change in pixel values of the image. The left graph shows sum of deviation from the starting frame and the right graph shows its derivative. In the left, the graph line is constant until around frame 50 then bend to linear growth. This trend shows that there is motion that starts around frame 50. After that the object inside the video moves. Before frame 50, the sum of deviation remains stable around 20,000 which means that no significant motion. The value does not fall to zero because some noise in the image. However, it is difficult to judge when the motion started by only the left graph. The right graph, which is its derivative, shows significant shift. The shifts indicate when the video changes from nothing happen to the piston have a motion. In this case, the threshold value for the change is 400. By such threshold, the motion was starting at frame 51 at which the trend in left graph shows well support.

Clog enhancement via image processing

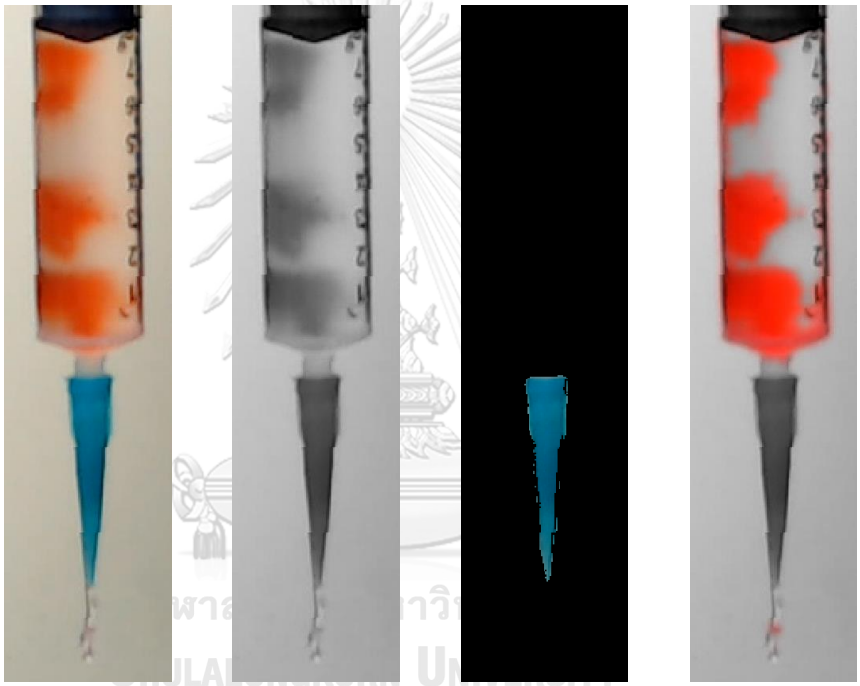

(a) (b) (c) (d)

Figure 50 (a) orignal image, (b) grayscale image, (c) nozzle mask, and (d) result image with enhanced high concentration gelatin

To gain more precise information, the image processing was used for detecting the clog. Apart from red color that mix to the high concentration gelatin, some of them dilute from high temperature in the lower concentration mixture. Thus, it is not clear to see the clogging. Furthermore, the clogging inside the nozzle is not easy to see as the nozzle is quite opaque.

To enhance the image, original image (a) was brought and then turned to grayscale (b). Next, the masking of nozzle (c) is created by selecting one frame and then uses color thresholding. After that, other two color thresholds are implemented on the area outside and inside the nozzle. The outside area is easily to detects the high concentration gelatin as it is red compared to the background. However, inside the nozzle, it is difficult for red color to go

through green material. Consequently, only darker green is seen from the red concentration gelatin that flows into the nozzle.

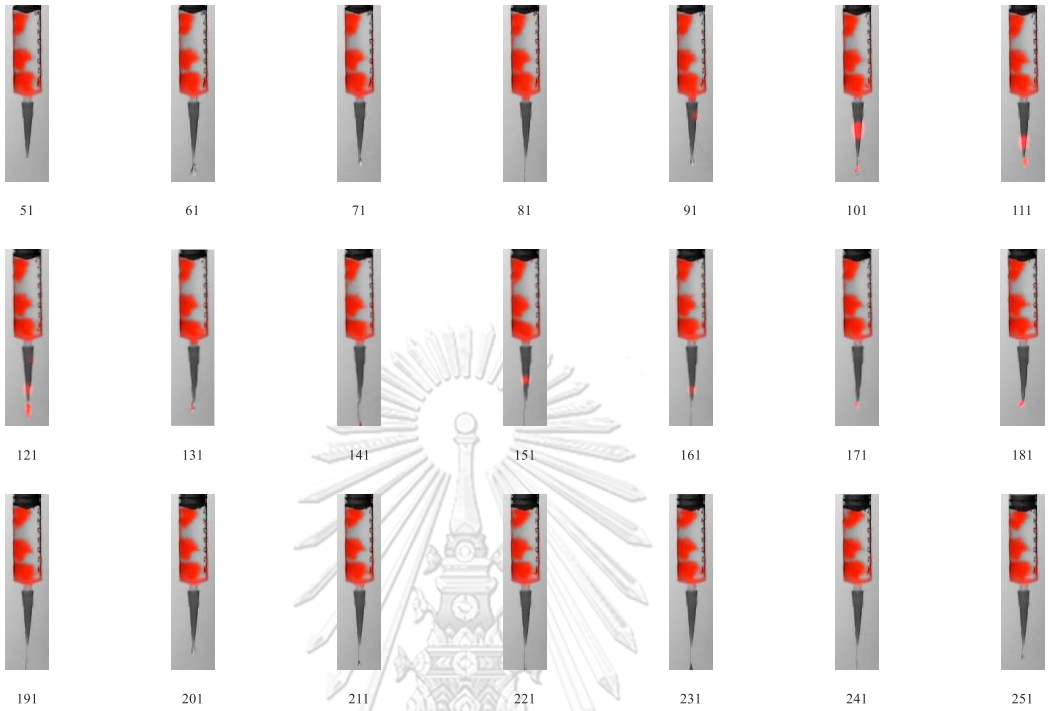

Figure 51 Sample of processed frame of the nozzle. The red color indicates high concentration gelatin. The clogging was happened when the high concentration gelatin (red) is inside the nozzle.

Figure 51 is the example of processed image. The gelatin inside the nozzle is enhanced by highlighting with glowing red. The background is then dropped to grayscale to boost the red of clogging. From this figure, it can be seen that some point of time high concentration gelatin was clogged inside the nozzle and then pushed out. For example, the frame 151, 161, 171, and 181 shows continuous motion of clog that flow through the nozzle.

Experimental result

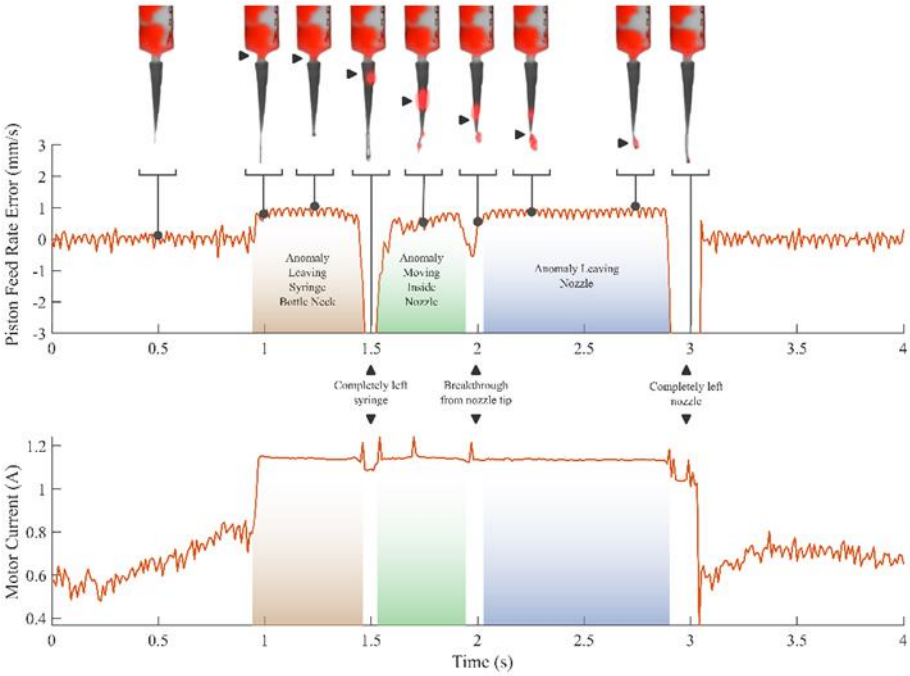

Figure 52 The illustration of intrinsic sensing: visibility of printing material. Anomaly-infested material is represented by a non-homogenous biogel formed by mixing concentrated biogel (red) in its regular counterpart(transparent). Piston feed rate error is calculated from the difference between the reference feed rate and the actual feed rate measured by the encoder. The trend of this parameter corresponds with the location of the anomaly which is illustrated by black triangles. The motor current is measured by the motor driver chip and is proportional to the force that the motor exerts.

In this experiment, a non-homogenous hydrogel mixture was extruded using the proposed technique; machine vision was used to capture the flow during extrusion. A video was synchronized with the signals monitored from the ram extruder's microcontroller. Throughout the extrusion of the non-homogenous hydrogel mixture, piston feed rate error and motor current were plotted over time (Figure 52).

At the beginning of the extrusion, regular hydrogel flowed through the nozzle and escaped through the tip of the nozzle. Feed rate error stabilized around the value of 0 mm/s whilst the motor current increased slowly. After 1 s, a small part of the highly concentrated gel was forced through the narrow area at the lowest section of the syringe. Due to an increase in resistance, the same pressure applied could not maintain the constant flow of the material anymore.

Consequently, both feed rate error and motor current sharply increased to around 1 mm/s and 1.2A, respectively. During the next 0.5 s period, a greater volume of the viscous gel was pushed through the bottleneck of the syringe, corresponding with the steadiness of the two variables at the raised values. At about 1.5 s, the concentrated gel detached from the main

body and slipped into the broadest part of the nozzle (uppermost). When the resistance at the bottleneck sharply dropped, the internal stress of the material in the syringe lowered instantly. Thereupon, the residual gel in the nozzle squirted out. This overflow resulted in a drastic drop in feed rate error and a slight drop in motor current. The detached gel in the nozzle then drifted down towards the tip. Thereby, more effort from the motor was required to push it through the smaller cross-sectional area. Hence, the feed rate error slowly increased while the motor current remained steady at an elevated level.

At roughly 2 s, part of the fragment began to escape through the nozzle tip. This process continued for almost 1 s, while both feed rate error and motor current were maintained at the ascended values. At around 2.9 s, the detached gel fully exited from the tip of the nozzle. The instant the pressure was released, the overflow of the material out of the nozzle brought about a sharp drop in feed rate error along with a small drop in motor current. This event was followed by a rapid decrease of the current in the next 0.2 s, approximately. without the presence of highly viscous gel in the syringe bottleneck and the nozzle. Feed rate error once again converged around the value of 0 mm/s, while the motor current dropped back and slightly fluctuated around 0.7 A.

As for the actual case of viscoelastic material, the flow is highly complex as the material possesses both properties of solid and fluid. The material needs to be compressed through the taper of the nozzle. As such, the deformation and flow of matter are very difficult to model. Furthermore, it is sensitive to disturbances such as temperature. It is also noted that even if the temperature is controlled, it is still challenging to guarantee that the temperature inside the syringe is uniform. This complication of rheology may reflect the pressure and flow.

In the demonstration, the proposed prototype can detect the difference in rheology as the material suddenly gains more viscosity and stiffness. In Figure 52, results show the potential usage of the thresholding method to detect clogging inside the nozzle. In the graph, the piston feed rate error of 0.5 mm/s can be used to detect anomalies. Such a technique may further be used in real applications to prevent print failure.

Furthermore, the signal that is demonstrated reflects the flushing completion when the clog is flushed out (Figure 52). The drastic drop in feed error is highly related to the breakthrough of the clog. Using the threshold technique, this event is easily detected. The proposed hardware has the potential to detect clogs in real time during the printing process and is also able to sense the completion of clog flushing.

Conclusion

In this dissertation, a novel actuation for LDM extrusion is proposed. Such actuation is capable for both pressure controlled and volumetric controlled extrusion. The main concept is using a ball screw and a dc motor. By controlling the current that flows through the dc motor, the pressure can be commanded. The volumetric controlled extrusion can be done by measuring the angular position of the motor and then applied a feedback position controlled loop. To evaluate the objective, the actual hardware is implemented. The performance of pressure measurement and control are evaluated by compressing the air. The sensitivity of measurement is 290.6 kPa/A, and the resolution of the hardware is 0.23 kPa. The line extrusion experiment was conducted for evaluation of volumetric controlled. The printed line of biogel, chocolate fudge, and silicone sealant via volumetric controlled gave the highest quality. All those linewidths have the lowest standard deviation compared to other pressure control. Furthermore, the proposed hardware also benefits from sensing the pressure along with the volumetric control. The experiment shows that the control signals from such hardware are correlated extrudability of the material. Thus, clogging can be sensed.

In conclusion, the successful implementation and comprehensive evaluations of the proposed actuation method mark a significant advancement in LDM extrusion technology. With its demonstrated capabilities in pressure and volumetric control, coupled with the ability to sense clogging, this innovative hardware opens new possibilities for precision and efficiency in LDM extrusion processes.

จุฬาลงกรณ์มหาวิทยาลัย
CHULALONGKORN UNIVERSITY

REFERENCES

1

[1] I. Gibson, D. W. Rosen, and B. Stucker, *Additive manufacturing technologies: Rapid prototyping to direct digital manufacturing* (Additive Manufacturing Technologies: Rapid Prototyping to Direct Digital Manufacturing). 2010, pp. 1-459.

[2] T. D. Ngo, A. Kashani, G. Imbalzano, K. T. Q. Nguyen, and D. Hui, "Additive manufacturing (3D printing): A review of materials, methods, applications and challenges," *Composites Part B: Engineering,* Review vol. 143, pp. 172-196, 2018, doi: 10.1016/j.compositesb.2018.02.012.

[3] M. Attaran, "The rise of 3-D printing: The advantages of additive manufacturing over traditional manufacturing," *Business Horizons,* Article vol. 60, no. 5, pp. 677-688, 2017, doi: 10.1016/j.bushor.2017.05.011.

[4] W. Gao *et al.*, "The status, challenges, and future of additive manufacturing in engineering," *CAD Computer Aided Design,* Article vol. 69, pp. 65-89, 2015, doi: 10.1016/j.cad.2015.04.001.

[5] J. Y. Lee, J. An, and C. K. Chua, "Fundamentals and applications of 3D printing for novel materials," *Applied Materials Today,* Review vol. 7, pp. 120-133, 2017, doi: 10.1016/j.apmt.2017.02.004.

[6] B. Berman, "3-D printing: The new industrial revolution," *Business Horizons,* Article vol. 55, no. 2, pp. 155-162, 2012, doi: 10.1016/j.bushor.2011.11.003.

[7] C. Weller, R. Kleer, and F. T. Piller, "Economic implications of 3D printing: Market structure models in light of additive manufacturing revisited," *International Journal of Production Economics,* Article vol. 164, pp. 43-56, 2015, doi: 10.1016/j.ijpe.2015.02.020.

[8] S. A. M. Tofail, E. P. Koumoulos, A. Bandyopadhyay, S. Bose, L. O'Donoghue, and C. Charitidis, "Additive manufacturing: scientific and technological challenges, market uptake and opportunities," *Materials Today,* Review vol. 21, no. 1, pp. 22-37, 2018, doi: 10.1016/j.mattod.2017.07.001.

[9] A. D. Valino, J. R. C. Dizon, A. H. Espera, Q. Chen, J. Messman, and R. C. Advincula, "Advances in 3D printing of thermoplastic polymer composites and nanocomposites," *Progress in Polymer Science,* Review vol. 98, 2019, Art no. 101162, doi: 10.1016/j.progpolymsci.2019.101162.

[10] S. Dul, L. Fambri, and A. Pegoretti, "Development of new nanocomposites for 3D printing applications," in *Structure and Properties of Additive Manufactured Polymer Components*, 2020, pp. 17-59.

[11] M. Rosenthal, C. Henneberger, A. Gutkes, and C. T. Bues, "Liquid Deposition Modeling: a promising approach for 3D printing of wood," *European Journal of Wood and Wood Products,* Article vol. 76, no. 2, pp. 797-799, 2018, doi:

10.1007/s00107-017-1274-8.

[12] M. F. C. De Andrade, R. C. Nonato, R. Bottini, and A. R. Morales, "Quality evaluation of solvent-cast 3D printing of poly(lactic acid) films," *Bulletin of Materials Science,* Article vol. 43, no. 1, 2020, Art no. 74, doi: 10.1007/s12034-019-2025-8.

[13] M. Z. Chaari, M. Abdelfatah, and C. Loreno, "A trial to convert a polymer FDM 3D printer to handle clay materials," *SN Applied Sciences,* Article vol. 4, no. 3, 2022, Art no. 68, doi: 10.1007/s42452-022-04937-w.

[14] S. N. Kwon, S. W. Kim, I. G. Kim, Y. K. Hong, and S. I. Na, "Direct 3D Printing of Graphene Nanoplatelet/Silver Nanoparticle-Based Nanocomposites for Multiaxial Piezoresistive Sensor Applications," *Advanced Materials Technologies,* Article vol. 4, no. 2, 2019, Art no. 1800500, doi: 10.1002/admt.201800500.

[15] D. Chimene, R. Kaunas, and A. K. Gaharwar, "Hydrogel Bioink Reinforcement for Additive Manufacturing: A Focused Review of Emerging Strategies," *Advanced Materials,* Review vol. 32, no. 1, 2020, Art no. 1902026, doi: 10.1002/adma.201902026.

[16] M. M. Rueda *et al.*, "Rheology and applications of highly filled polymers: A review of current understanding," *Progress in Polymer Science,* Review vol. 66, pp. 22-53, 2017, doi: 10.1016/j.progpolymsci.2016.12.007.

[17] S. M. Rangappa, J. Parameswaranpillai, S. Siengchin, and T. Ozbakkaloglu, *Elastomer Blends and Composites: Principles, Characterization, Advances, and Applications* (Elastomer Blends and Composites: Principles, Characterization, Advances, and Applications). 2022, pp. 1-420.

[18] E. J. Courtial *et al.*, "Silicone rheological behavior modification for 3D printing: Evaluation of yield stress impact on printed object properties," *Additive Manufacturing,* Article vol. 28, pp. 50-57, 2019, doi: 10.1016/j.addma.2019.04.006.

[19] X. Xiao *et al.*, "Solvent evaporation induced fabrication of porous polycaprolactone scaffold via low-temperature 3D printing for regeneration medicine researches," *Polymer,* Article vol. 217, 2021, Art no. 123436, doi: 10.1016/j.polymer.2021.123436.

[20] J. J. Nijdam, D. LeCorre-Bordes, A. Delvart, and B. S. Schon, "A rheological test to assess the ability of food inks to form dimensionally stable 3D food structures," *Journal of Food Engineering,* Article vol. 291, 2021, Art no. 110235, doi: 10.1016/j.jfoodeng.2020.110235.

[21] K. Bouzidi, D. Chaussy, A. Gandini, R. Bongiovanni, and D. Beneventi, "3D printable fully biomass-based composite using poly(furfuryl alcohol) as binder and cellulose as a filler," *Carbohydrate Polymers,* Article vol. 293, 2022, Art no. 119716, doi: 10.1016/j.carbpol.2022.119716.

[22] A. Pricci, M. D. De Tullio, and G. Percoco, "Semi-analytical models for non-Newtonian fluids in tapered and cylindrical ducts, applied to the extrusion-based additive manufacturing," *Materials and Design,* Article vol. 223, 2022, Art no.

111168, doi: 10.1016/j.matdes.2022.111168.

[23] S. A. Tronvoll, S. Popp, C. W. Elverum, and T. Welo, "Investigating pressure advance algorithms for filament-based melt extrusion additive manufacturing: theory, practice and simulations," *Rapid Prototyping Journal,* Article vol. 25, no. 5, pp. 830-839, 2019, doi: 10.1108/RPJ-10-2018-0275.

[24] X. Ang, J. Y. Tey, W. H. Yeo, and K. P. Y. Shak, "A review on metallic and ceramic material extrusion method: Materials, rheology, and printing parameters," *Journal of Manufacturing Processes,* Review vol. 90, pp. 28-42, 2023, doi: 10.1016/j.jmapro.2023.01.077.

[25] B. A. Morris, *The Science and Technology of Flexible Packaging: Multilayer Films from Resin and Process to End Use, Second Edition* (The Science and Technology of Flexible Packaging: Multilayer Films from Resin and Process to End Use, Second Edition). 2022, pp. 1-761.

[26] P. Hajikarimi and F. Moghadas Nejad, *Applications of Viscoelasticity: Bituminous Materials Characterization and Modeling*. Elsevier, 2021, pp. 27-61.

[27] J. A. Epaarachchi, "The effect of viscoelasticity on fatigue behaviour of polymer matrix composites," in *Creep and Fatigue in Polymer Matrix Composites*, 2010, pp. 492-513.

[28] L. Zou, J. Yuan, X. Liu, J. Li, P. Zhang, and Z. Niu, "Burgers viscoelastic model-based variable stiffness design of compliant clamping mechanism for leafy greens harvesting," *Biosystems Engineering,* Article vol. 208, pp. 1-15, 2021, doi: 10.1016/j.biosystemseng.2021.05.007.

[29] A. Mantelli, M. Levi, S. Turri, and R. Suriano, "Remanufacturing of end-of-life glass-fiber reinforced composites via UV-assisted 3D printing," *Rapid Prototyping Journal,* Article vol. 26, no. 6, pp. 981-992, 2020, doi: 10.1108/RPJ-01-2019-0011.

[30] A. Das, E. L. Gilmer, S. Biria, and M. J. Bortner, "Importance of Polymer Rheology on Material Extrusion Additive Manufacturing: Correlating Process Physics to Print Properties," *ACS Applied Polymer Materials,* Review vol. 3, no. 3, pp. 1218-1249, 2021, doi: 10.1021/acsapm.0c01228.

[31] A. U. Rehman and J. H. Kim, "3d concrete printing: A systematic review of rheology, mix designs, mechanical, microstructural, and durability characteristics," *Materials,* Review vol. 14, no. 14, 2021, Art no. 3800, doi: 10.3390/ma14143800.

จุฬาลงกรณ์มหาวิทยาลัย
Chulalongkorn University

VITA

NAME	Kantawatchr Chaiprabha
DATE OF BIRTH	20 September 1999
PLACE OF BIRTH	
INSTITUTIONS ATTENDED	Chulalongkorn University
HOME ADDRESS	
PUBLICATION	- Chaiprabha, K.; Chanchareon, R. Innovative Smart Drilling with Critical Event Detection and Material Classification. J. Manuf. Mater. Process. 2023, 7, 155. - Chaiprabha, K.; Chancharoen, R. A Deep Trajectory Controller for a Mechanical Linear Stage Using Digital Twin Concept. Actuators 2023, 12, 91.

จุฬาลงกรณ์มหาวิทยาลัย
CHULALONGKORN UNIVERSITY